Resonance Energy Transfer Imaging of Phospholipid Vesicle Interaction with a Planar Phospholipid Membrane

Undulations and Attachment Sites in the Region of Calcium-mediated Membrane–Membrane Adhesion

WALTER D. NILES,* JOHN R. SILVIUS,‡ and FREDRIC S. COHEN*

From the *Department of Molecular Biophysics and Physiology, Rush Medical College, Chicago, Illinois 60612; and ‡Department of Biochemistry, McGill University, Montréal, Quebec H3G 1Y6, Canada

ABSTRACT Membrane fusion of a phospholipid vesicle with a planar lipid bilayer is preceded by an initial prefusion stage in which a region of the vesicle membrane adheres to the planar membrane. A resonance energy transfer (RET) imaging microscope, with measured spectral transfer functions and a pair of radiometrically calibrated video cameras, was used to determine both the area of the contact region and the distances between the membranes within this zone. Large vesicles (5–20 μm diam) were labeled with the donor fluorophore coumarin-phosphatidylethanolamine (PE), while the planar membrane was labeled with the acceptor rhodamine-PE. The donor was excited with 390 nm light, and separate images of donor and acceptor emission were formed by the microscope. Distances between the membranes at each location in the image were determined from the RET rate constant (k_t) computed from the acceptor:donor emission intensity ratio. In the absence of an osmotic gradient, the vesicles stably adhered to the planar membrane, and the dyes did not migrate between membranes. The region of contact was detected as an area of planar membrane, coincident with the vesicle image, over which rhodamine fluorescence was sensitized by RET. The total area of the contact region depended biphasically on the Ca^{2+} concentration, but the distance between the bilayers in this zone decreased with increasing [Ca^{2+}]. The changes in area and separation were probably related to divalent cation effects on electrostatic screening and binding to charged membranes. At each [Ca^{2+}], the intermembrane separation varied between 1 and 6 nm within each contact region, indicating membrane undulation prior to adhesion. Intermembrane separation distances ≤2 nm were localized to discrete sites that formed in an ordered arrangement throughout the contact region. The area of the contact region occupied by these punctate attachment sites was increased at high [Ca^{2+}]. Membrane fusion may be initiated at these sites of closest membrane apposition.

INTRODUCTION

Membrane fusion is a key mechanism underlying many cellular processes, including exocytosis, intracellular membrane trafficking, and fertilization, as well as pathological events such as the infection of cells by bacteria and viruses (White, 1992). In fusion, two phospholipid membranes, each demarcating separate aqueous compartments, meld into a contiguous lamella, and compartments initially delineated by the original membranes are joined (Zimmerberg et al., 1993). Although these different biological processes are regulated by distinct sets of proteins (Bennett and Scheller, 1993), membrane fusion, the common feature controlled by these proteins, is essentially the coalescence of two highly anisotropic, viscoelastic fluids.

We developed a model system in which phospholipid vesicles fuse with a planar phospholipid membrane to determine the mechanics and energetics

Address correspondence to Walter D. Niles at his present address, Department of Pharmacology, University of Illinois School of Medicine, 835 South Wolcott Street, MSB 911, Room E-403, Chicago, Illinois 60612. Fax, (312) 996-1225; E-mail, wniles@uic.edu

J. GEN. PHYSIOL. © The Rockefeller University Press • 0022-1295/96/03/329/23 $2.00
Volume 107 March 1996 329–351

common to all biological occurrences of membrane fusion (Zimmerberg et al., 1980; Cohen et al., 1980). Fusion occurs in at least two experimentally resolvable stages. In the first stage, the vesicle approaches and binds stably to the planar membrane (Akabas et al., 1984), but the lipid bilayers do not generally coalesce (Niles and Cohen, 1987). The hydration of the polar membrane surfaces (LeNeveu et al., 1976) and elastic properties such as bending and surface energies (Helfrich, 1978) limit their close approach and contact. Membranes containing anionic lipids require Ca^{2+} or other divalent cations to form the adherent, prefusion state (Akabas et al., 1984). This stage is long lived, because bilayers are stable (Evans and Waugh, 1977; Needham and Haydon, 1983) and externally applied energy, such as osmotic swelling of the vesicles (Cohen et al., 1980), is necessary to drive the membranes into the second stage, in which the two membranes mix into a single lipid bilayer and the vesicle contents are released to the opposite side of the planar membrane.

The extent of the adhesion interaction between membranes in the prefusion state has remained uncertain. Both the fraction of the vesicle's surface area close enough to the planar membrane to be considered in contact and the distance between the membranes in the contact region have remained unknown. These parameters affect the ability of an osmotic water flux across the planar membrane to generate an intravesicular hydrostatic pressure sufficient to cause fusion (Niles et al., 1989). In addition, certain membrane mixtures, such as those containing concave-shaped lipids like phosphatidylethanolamine (PE) in the two facing leaflets, sometimes undergo monolayer mixing to form a partially fused intermediate (Chernomordik et al., 1995), although we have found contacting membranes to remain separate and distinct without mixing of the apposed monolayers (Niles and Cohen, 1987). Because the conformations of membranes during stages of fusion define the process, the structure of membranes in the region of contact between the vesicle and the planar bilayer in the adherent state is of interest. Distortions from smoothness between adhering membrane surfaces could impart stresses needed for the localized membrane breakage leading to fusion. It remains to be determined whether distinct conformations of membrane exist at discrete stages of fusion or whether membrane reorganization is so fast, random, and complex that exactly reproducible lipid configurations do not exist but rather are the strange attractors of a dynamical system (Ruelle, 1989). Nonetheless, one discrete stage, adhesion, has been found and we characterize it in this paper.

To observe adhesion as well as other long-lived structures of membranes during fusion, we have turned to resonance energy transfer (RET) imaging microscopy (Herman, 1989; Ludwig et al., 1992; Niles et al., 1993). To develop this new method for the measurement of molecular-scale distances, we have initially focused on stationary interactions between vesicular and planar membranes in the region of contact that forms prior to fusion. The donor probe was a dimethylaminocoumarin-4-acetyl group covalently attached to the headgroup amine of PE (cou-PE) (Silvius et al., 1987) and the acceptor probe was Lissamine rhodamine B-PE (rho-PE) (Massari et al., 1988). The donor was present in the vesicle membrane, and the acceptor was placed in the planar membrane as schematized in Fig. 1 *A*. The donor was directly excited, and the fluorescence emissions of both donor and acceptor probes were simultaneously observed. The two separate images were overlayed in spatial correspondence and their intensities were used to calculate a ratio image that indicated the rate constant of RET (k_t) at each location. As k_t varies with the distance of separation between the probes (Förster, 1948; Drake et al., 1991), the ratio image determined both the contact area of the vesicle and planar membrane and the separation distances between them. We examined the RET ratio images for indicators of membrane conformational intermediates of fusion and characterized the contact region in terms of the forces necessary to bring membranes into close apposition. Structures we found may provide the nucleation sites necessary to initiate membrane fusion.

THEORY

RET occurs between two fluorescent molecules when a donor fluorophore, which is directly excited by the illuminating excitation light, is located close to an unexcited acceptor fluorophore. It originates from the interaction of the wavefunction of the excited donor with the wavefunction of the ground-state acceptor (Förster, 1948). This occurs when the donor emission and acceptor absorption spectra overlap, and the excited donor's emission dipole is not perpendicular to the unexcited acceptor's absorption dipole (Dale and Eisinger, 1974). The RET rate constant (k_t) indicates the rate at which the donor's excitation probability is transferred to the acceptor (Förster, 1948). For two probes separated by a distance R,

$$k_t = 1/\tau_D (R/R_o)^{-6}, \quad (1)$$

where τ_D is the lifetime of the excited state of the donor in the absence of RET and R_o is the Förster critical distance. R_0, the distance at which the excited donor transfers its energy to the acceptor with a probability of 1/2, is given (in nanometers) by

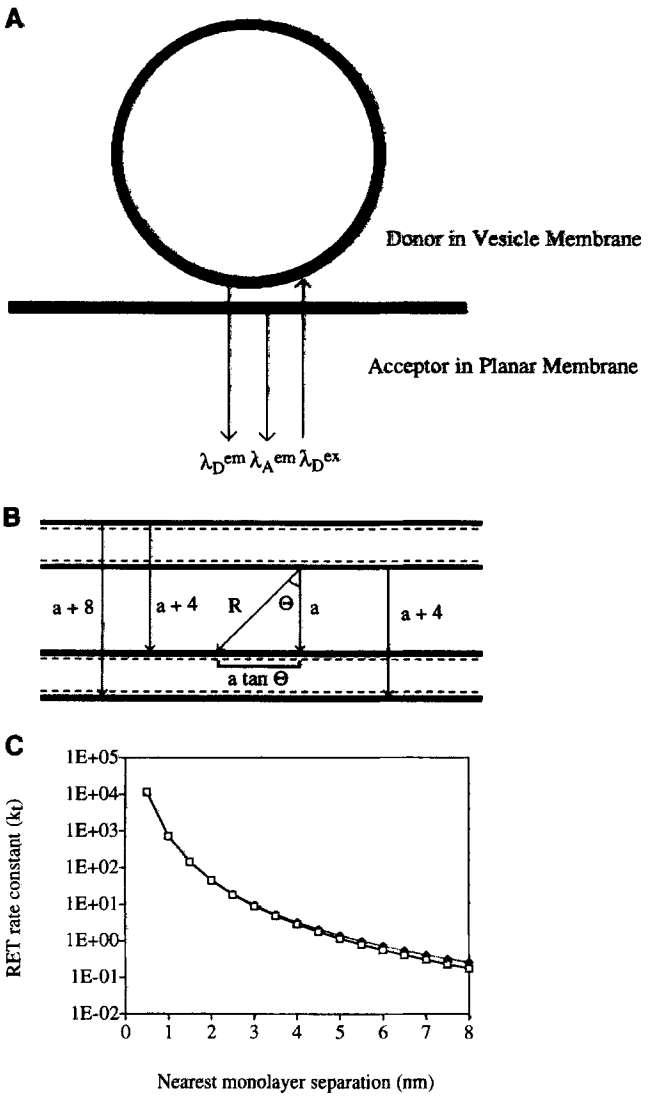

FIGURE 1. RET imaging of the region of contact between vesicular and planar membranes. (*A*) Locations of RET fluorescent probes. The vesicle membrane is labeled with the donor cou-PE and the planar membrane is labeled with the acceptor rho-PE. Vesicles are introduced to the planar membrane on the *cis* side. Epi-illumination and observation are done through the *trans* compartment. The donor is excited with 390 nm light from a monochromator. The light emitted by the donor and acceptor fluorophores through the *trans* compartment is collected by the objective. (*B*) Geometric arrangement of probes and calculation of RET rate constant. The donor is confined to the two top planes representing the two monolayers of the vesicle membrane. The acceptor is located in the bottom two monolayers of the planar membrane. We assumed that each probe was located at the amino end of the 0.5-nm long headgroup and resided at the headgroup–water interface. The normal separation between the probes in the monolayers of the same membrane was 4 nm to account for the 3-nm thickness of the hydrocarbon core (the idealized junction between the headgroup and tail regions of each monolayer is denoted by a dashed line). The nearest approach of any donor-acceptor pair is *a*. The RET rate constant is calculated for any point in the donor plane using the normal separation distance and the radial vector **R** to each acceptor, where $R = |\mathbf{R}|$ is the distance of separation between the donor probe and a particular acceptor in one of the opposite monolayers. The total amount of RET between the donor and all the acceptors in the opposite plane is obtained by sweeping the angle between **R** and the normal, Θ, from 0 to $\pi/2$, and by sweeping **R** around the normal by 2π radians. The unit increment of circular area in the acceptor plane around the normal at *a* is $2\pi a^2 \tan\Theta\, d(\tan\Theta)$. From Eq. 1,

$$k_t = [(R_o)^6/\tau_D]\, 2\pi a^2 \int_0^{\pi/2} R^{-6} \tan\Theta\, d(\tan\Theta) =$$

$$[(R_o)^6/\tau_D]\, 2\pi a^2 \int_0^{\pi/2} (a \sec\Theta)^{-6} \tan\Theta \sec^2\Theta\, d\Theta.$$

The results are given in Eq. 4a for a single pair of donor and acceptor planes at separation a and in Eq. 4b for all four possible pairs of donor and acceptor planes. (*C*) Differences of the RET rate constant k_t obtained using Eq. 4a (*open boxes*) and 4b (*filled diamonds*). k_t is plotted as a function of the separation distance between the nearest pair of donor and acceptor monolayers, *a*. Differences between the two expressions are only significant at relatively large separation (>5 nm). Thus, we used Eq. 4a to express the geometrical dependence of k_t for computational simplicity.

$$R_o = 979[\kappa^2 \Phi_D n^{-4} J(\lambda)]^{1/6}, \quad (2)$$

where κ^2 is the geometrical orientation factor describing the average alignment between the transition dipoles of the acceptor and the excited donor, Φ_D is the quantum yield of the donor in the absence of acceptor, n is the refractive index of the medium in which the electromagnetic wave propagates, and $J(\lambda)$ is the spectral overlap integral (Förster, 1948; Herman, 1989). We determined R_o spectrofluorimetrically in separate experiments with liposomes labeled by the phospholipid probes (Estep and Thompson, 1979; Wolber and Hudson, 1979; Snyder and Friere, 1982) as well as by measuring the parameters of Eq. 2.

In vesicle-planar membrane experiments, RET was determined as the sensitization intensity ratio $\Delta I_A/I_D$ calculated at each image location, where ΔI_A is the acceptor fluorescence intensity sensitized by RET from the donor, and I_D is the donor emission intensity (Herman, 1989; Ludwig et al., 1992). The ratio image provided a pixel-by-pixel evaluation of k_t, which is related to $\Delta I_A/I_D$ by the photophysical reaction described below. We present a complete derivation tacitly assumed, but never explicitly shown in prior treatments (Brand and Withold, 1967; Herman, 1989; Ludwig et al., 1992). We assume that k_D^{ex} and k_A^{ex} are the excitation rates of ground-state donors *D* and acceptors *A* by the illuminating light and that k_D^f and k_A^f are the fluorescence rates of excited-state donors *D** and acceptors *A**. The equations

$$D \xrightarrow{k_D^{ex}} D^*$$

$$A \xrightarrow{k_A^{ex}} A^*$$

$$D^* + A \xrightarrow{k_t} D + A^*$$

$$D^* \xrightarrow{k_D^f} D$$

$$A^* \xrightarrow{k_A^f} A$$

describe the excitation, RET and fluorescence processes. The rates of formation and decay of the excited states are

$$dD^*/dt = k_D^{ex} D - (k_D^f + k_t A)\, D^* \text{ and}$$

$$dA^*/dt = (k_A^{ex} + k_t D^*)\, A - k_A^f A^*$$

with the assumptions that the RET process is identical for all donor-acceptor pairs and that probe pairs interact independently of other probe pairs in the specimen (Förster, 1948). The total surface area densities of donor and acceptor are $D_T = D + D^*$ and $A_T = A + A^*$, and we assume that only a small fraction of acceptors are excited at any instant of time such that $A \cong A_T$. At steady state,

$$D^* = k_D^{ex} D_T / (k_D^{ex} + k_D^f + k_t A_T) \text{ and}$$

$$A^* = (k_A^{ex} + k_t D^*)\, A_T / k_A^f.$$

The emission intensities are $I_D = k_D^f D^*$ for the donor, and $I_A = k_A^f A^*$ for the acceptor. The background intensity of the acceptor due to direct excitation by illumination is $I_A^0 = k_A^{ex} A_T$, so that the intensity of acceptor emission sensitized to fluorescence by RET from the donor is $\Delta I_A = I_A - I_A^0 = k_t D^* A_T$. Thus, the ratio of sensitized acceptor to donor intensities is

$$\Delta I_A / I_D = k_t A_T / k_D^f \tag{3}$$

and, at each location in the ratio image, the sensitization ratio is proportional to the RET rate constant k_t.

Intermembrane separation distances at each image location were extracted from k_t by assuming that each membrane consisted of two infinite parallel planes corresponding to the two monolayers comprising each bilayer as depicted in Fig. 1 *B*. The donor probes were distributed randomly at surface density D_T on the surfaces of the two vesicular monolayers, and the acceptor probes were similarly arranged at density A_T in the two monolayers of the planar membrane. The headgroups of the two facing monolayers of the apposed vesicular and planar membranes were separated by a normal distance (the separation distance along the normal or perpendicular interplane distance) of a, the minimum separation between any donor and acceptor pair. As the probe moieties were at the amino end of each labeled lipid's 0.5 nm long headgroup, we assumed that each probe lay at the headgroup-water interface and the measured intermembrane separations were distances between these interfaces. The RET rate constant k_t for any donor was found by integrating Eq. 1 over the surface area of the opposing planar array of acceptors (Kuhn, 1970; Gibson and Lowe, 1979) to yield

$$k_t = (R_o)^6 \pi / (2\tau_D a^4). \tag{4a}$$

Each donor interacts with two parallel planes of acceptors separated by 4 nm (the bilayer thickness), however, and, at each spatial location in the image, the acceptors are sensitized to fluorescence by interaction with two planar arrays of donors. The RET rate constant for all interactions is given by

$$k_t = [(R_o)^6 \pi / 2\tau_D]\, [1/a^4 + 2/(a+4)^4 + 1/(a+8)^4]. \tag{4b}$$

In Fig. 1 *C*, k_t (normalized by $(R_o)^6 \pi / 2\tau_D$) is plotted as a function of separation distance a as predicted by both Eqs. 4a and 4b. Contributions from the latter two terms in the denominator of Eq. 4b are appreciable only at separations $>> R_o$. Thus, we used Eq. 4a to determine intermembrane separation distances in the ratio images.

MATERIALS AND METHODS

Determination of Fluorescence and RET Properties of Coumarin- and Rhodamine-PE

Accurate interpretation of RET ratio images as distances between vesicular and planar membranes required determination of the fluorescence and energy transfer characteristics of the donor and acceptor probes. Because cou-PE and rho-PE have not been used as an RET pair in microscopy, we measured their fluorescence characteristics in liposomes in order to determine R_0 by both experiment and calculation. As these fluorescence properties are needed to obtain the microscopy results, we present the fluorimetric data in this section, together with the procedures used in their measurement.

Phospholipids. The fluorescently labeled phospholipids, 1-palmitoyl, 2-oleoyl-*sn*-glycero-3-phosphoethanolamine-*N*-[7-dimethylaminocoumarin-4-acetyl], and 1,2-dioleoyl-*sn*-glycero-3-phosphoethanolamine-*N*-[lissamine rhodamine B sulfonyl], rho-PE, were used as donor and acceptor probes, respectively. Cou-PE was synthesized by reaction of PE with succinimidyl 7-dimethylaminocoumarin-4-acetate according to published procedures (Silvius et al., 1987). Rho-PE was purchased commercially (Avanti Polar Lipids, Inc., Pelham, AL). Cou-PE and rho-PE in $CHCl_3$ stock solutions remained stable for ~30 d at −20°C as checked by thin-layer chromatography on silica gel plates run in $CHCl_3$/methanol/NH_4OH (65/32/3 by vol) or $CHCl_3$/methanol/CH_3COOH (65/30/5), respectively. The unlabeled phospholipids egg lecithin (PC), dioleoyl PE, and brain phosphatidylserine (PS) were purchased commercially (Avanti Polar Lipids, Inc.), as were cholesterol and triolein (Sigma Chemical Co., St. Louis, MO).

Detergent-dialysis liposomes. The fluorescence and RET properties of the dyes were determined using detergent dialysis liposomes. To obtain the desired mole fractions of labeled lipids in the liposomes, aliquots of chloroform stock solutions of the probes were mixed with a chloroform solution consisting of unlabeled 6:1 (4:1 PC:PS):cholesterol (by mole fraction). The chloroform was dried under a stream of Ar and then in vacuo for 45 min. The dried lipid mixture (6.8 μmol total) was resuspended in 0.5 ml of 20 mM cholic acid, 120 mM NaCl, 10 mM HEPES, 3 mM $MgCl_2$, 1 mM EDTA, pH 7.4, with vortexing, and the suspension was sonicated to clarity in a bath sonicator at room temperature. The suspension was placed in a dialysis bag (1 × 7 cm, SpectraPor 2, Spectrum Medical Industries, Los Angeles, CA) and dialyzed against 1 liter of the buffer solution 120 mM NaCl, 10 mM HEPES, 3 mM $MgCl_2$, 1 mM EDTA, pH 7.4. The buffer was replaced every 12 h for five changes to remove the cholate and to produce a cloudy suspension of liposomes that should have been homogeneous with a diameter of ~100 nm (Szoka and Papahadjopoulos, 1980). Cholesterol was included in these liposomes because sterol was used in the vesicle-planar membrane experiments, and it is known to affect rho-PE fluorescence (Massari et al., 1988; MacDonald, 1990).

Spectrofluorimetry. Absorption spectra and quantum distribution functions of cou-PE and rho-PE emission (see Fig. 2 *A*) were measured with the fluorescently labeled detergent dialysis liposomes in a spectrofluorimeter (SPF 500C, SLM-Aminco, Urbana, IL) equipped with automated polarization analysis filters. 25 μl of the liposome suspension, containing 0.1, 0.2, 0.5, 1.0, or 2.0 mol% of either probe, was added to 3 ml of the buffer solution in a 1 × 1 × 4 cm quartz cuvette. The temperature of the cuvette holder was held at 25°C, and the cuvette was stirred continuously with a Teflon-coated flea. Excitation and emission wavelengths

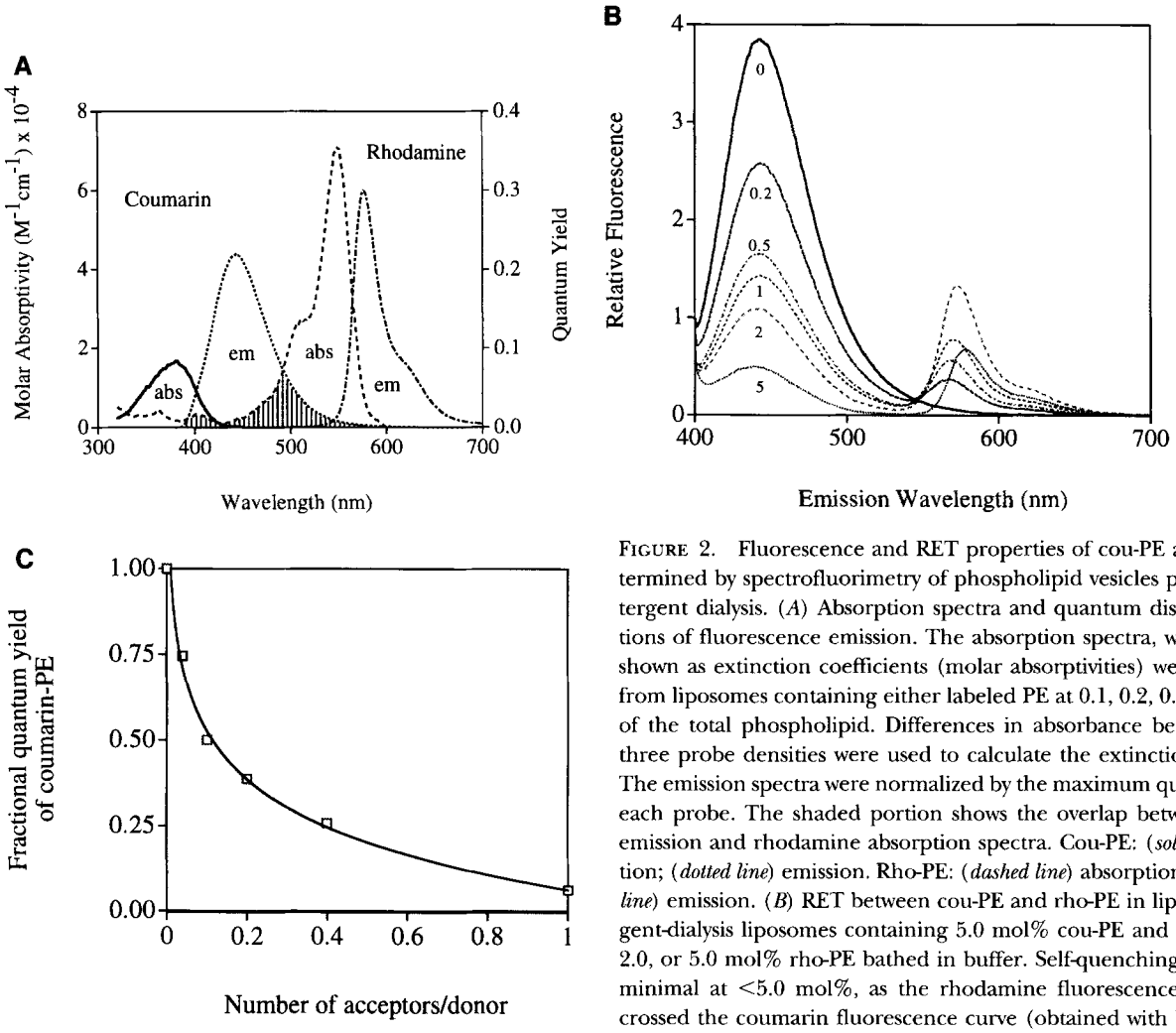

FIGURE 2. Fluorescence and RET properties of cou-PE and rho-PE determined by spectrofluorimetry of phospholipid vesicles prepared by detergent dialysis. (*A*) Absorption spectra and quantum distribution functions of fluorescence emission. The absorption spectra, with amplitudes shown as extinction coefficients (molar absorptivities) were determined from liposomes containing either labeled PE at 0.1, 0.2, 0.5, or 1.0 mol% of the total phospholipid. Differences in absorbance between the first three probe densities were used to calculate the extinction coefficients. The emission spectra were normalized by the maximum quantum yield of each probe. The shaded portion shows the overlap between coumarin emission and rhodamine absorption spectra. Cou-PE: (*solid line*) absorption; (*dotted line*) emission. Rho-PE: (*dashed line*) absorption; (*dashed-dotted line*) emission. (*B*) RET between cou-PE and rho-PE in liposomes. Detergent-dialysis liposomes containing 5.0 mol% cou-PE and 0, 0.2, 0.5, 1.0, 2.0, or 5.0 mol% rho-PE bathed in buffer. Self-quenching of rho-PE was minimal at <5.0 mol%, as the rhodamine fluorescence intensities all crossed the coumarin fluorescence curve (obtained with liposomes containing no rho-PE) at the same wavelength. At 5 mol%, the crossover wavelength was red-shifted, indicating self-quenching of rhodamine fluorescence. RET measurements with probe mole percentages <5% were not significantly affected by self-quenching. (*C*) Rho-PE quenching of cou-PE fluorescence by RET in liposomes. For each emission spectrum of cou- and rho-PE colabeled liposomes, the coumarin fluorescence intensity at 440 nm was divided by the 440-nm intensity obtained with liposomes labeled only with 5 mol% coumarin-PE. This determined Φ_{DA}/Φ_D ratios plotted against the rhodamine:coumarin ratio for each labeled liposome preparation. The curve, obtained by non-linear regression, is $\Phi_{DA}/\Phi_D = 0.087\ (f)^{-0.672}$ ($R^2 = 0.91$). R_0, determined from the surface density of rho-PE (0.00563) where $\Phi_{DA}/\Phi_D = 0.5$, was 3.211 ± 0.301 nm.

TABLE I

Absorption and Emission Characteristics of Coumarin- and Rhodamine-labeled PE

	Coumarin-PE		Rhodamine-PE
Absorption maximum (nm)	381		549
Molar absorptivity maximum (M^{-1}-cm^{-1})	1.68×10^4		7.13×10^4
Emission maximum (nm)	443		570
Quantum yield	0.277		0.308
Emission anisotropy r	-0.0496 ± 0.0027		-0.1150 ± 0.063
Axial depolarization factor $<d_i^x>$	-0.353 ± 0.052		-0.411 ± 0.147
κ^2 minimum		0.3 to 0.4	
κ^2 maximum		0.8 to 0.9	
Spectral overlap integral J(λ) (cm^6-mol^{-1})		$3.841 \pm 0.082 \times 10^{-14}$	

were scanned at 1 nm/0.25 s and the intensity data was collected by computer. Each fluorescence spectrum was obtained simultaneously with an absorbance reference spectrum. The quantum distribution function of emission for each probe in Fig. 2 *A* was obtained by correcting the measured fluorescence spectrum for the absorbance of the sample at each wavelength (Brand and Withold, 1967). The molar absorptivities (extinction coefficients) at each wavelength were calculated from differences between absorption spectra obtained with mole percentages of label between 0.1 and 0.5%. The photomultiplier tubes and gain circuitry of the fluorimeter were standardized with an aqueous solution of 35 μM 6-carboxyfluorescein, which has a known quantum yield of 0.95 at 517 nm (Campbell and Dwek, 1981). The quantum yields of cou-PE and rho-PE, measured relative to the quantum yield standard 4 mg/ml quinine sulfate in 0.5 N H_2SO_4 (Brand and Withold, 1967; Campbell and Dwek, 1981), were 0.28 and 0.30. Data from these experiments used in the calculation of R_0 are shown in Table I.

Spectral overlap integral. We evaluated the overlap integral between the cou-PE emission and rho-PE absorption spectra of Fig. 2 *A*. The spectral overlap integral $J(\lambda)$ is $\int \epsilon(\lambda) f(\lambda) \lambda^4 d\lambda$, where $\epsilon(\lambda)$ is the molar absorptivity (extinction coefficient) of the acceptor at wavelength λ (in $M^{-1}cm^{-1}$) and $f(\lambda)d\lambda = F(\lambda)d\lambda / \int F(\lambda)d\lambda$, the emission intensity of the donor in the interval $[\lambda, \lambda + d\lambda]$ normalized by the total total fluorescence intensity (Brand and Withold, 1967; Herman, 1989). We obtained $J(\lambda) = 3.841$ (± 0.082 SE) $\times 10^{-14}$ cm^6-mol^{-1}.

Fluorescence polarization analysis. The geometrical orientation factor κ^2, from Eq. 2, was determined from the emission polarization anisotropies (r) of the probes contained in detergent dialysis liposomes. Each sample was excited with vertically polarized light and the emission components were measured in the vertical and horizontal directions of linear polarization. Cou-PE, present in the liposomes at either 0.5 or 2.0 mol%, was excited at 390 nm and rho-PE, present in different liposomes at the same molar percentage, was excited at 540 nm. The emission wavelength was scanned twice from 400 to 700 nm, once with the vertical polarizer in the emission path to obtain I_{VV} and then with the horizontal polarizer to obtain I_{VH}. After correction for the polarization transfer functions, the r was computed at each emission wavelength as $(I_{VV} - I_{VH})/(I_{VV} + 2\ I_{VH})$ (Dale and Eisinger, 1974). Our measured emission anisotropies of cou-PE and rho-PE are listed in Table I. Both indicate orientational freedom of the headgroup-attached probes.

We determined κ^2 from the axial depolarization factors d_i^x, which describe the change in scalar product of a fluorescent probe's transition moment when it spatially reorients after excitation but prior to emission (Dale and Eisinger, 1974; Dale et al., 1979). In the absence of RET, $<d_i^x> = (2.5\ r)^{1/2}$ (Dale and Eisinger, 1974). The RET axial depolarization factor d_T was measured in detergent dialysis liposomes colabeled with cou- and rho-PE at 0.5 and 1.0 mol% by exciting with 390 nm vertically polarized light and scanning the emission wavelength from 400 to 700 nm. We determined minimum and maximum ranges of κ^2 from published contour plots of axial depolarization factors (Dale and Eisinger, 1974). As shown in Table I, these measurements narrowed κ^2 from its possible range of [0, 4] to [0.35, 0.85], which improved the precision of our calculated estimate of R_0. This range of κ^2 is consistent with the often-assumed random orientation value of 2/3 (Dale and Eisinger, 1974), in accord with free rotation of the headgroup probes. Control experiments showed no effect of Ca^{2+}-induced vesicle aggregation on the geometrical factors.

Concentration-quenching of cou-PE and rho-PE fluorescence. We measured self quenching of probe fluorescence in detergent dialysis liposomes separately labeled with a single probe at 0.2, 0.5, 1.0, 2.0, and 5.0 mol%. Cou-PE was excited at 390 nm and the emission at 450 nm was measured, while rho-PE was excited at 570 nm and the emission at 590 nm was recorded. To determine self-quenching, the emission intensities recorded for the intact liposomes (F) were compared with the intensities (F_∞) obtained at the same wavelengths after disruption of the liposomes in 0.5% sodium dodecyl sulfate, which did not alter the fluorescence of either probe. The amount of self-quenching was calculated as $1.0 - F/F_\infty$. We found that cou-PE at 5 mol% was self-quenched by ~15%, while rho-PE over the range of 1.0 to 5.0 mol% underwent self-quenching from 20 to 80%.

Determination of the Förster critical distance R_0. We experimentally determined the R_0 for the cou-/rho-PE dye pair by measuring the quenching of cou-PE emission intensity at 440 nm by rho-PE in the same liposomes. The cou-PE molar percentage was fixed at 5 mol% in all liposomes. Separate batches of cou-PE-labeled liposomes were made containing 0, 0.2, 0.5, 1.0, 2.0, or 5.0 mol% rho-PE. The cou-PE was excited at 390 nm and the emission wave-

length was scanned from 400 to 700 nm to detect the fluorescence of both probes (see Fig. 2 *B*). RET between coumarin and rhodamine in liposomes was minimally affected by self-quenching of either probe except at 2 and 5 mol% rho-PE, where the wavelength of peak rhodamine emission was shifted from 567.3 nm to 572.1 nm.

To determine R_0 from the data in Fig. 2 *B*, we divided the cou-PE emission intensity at 440 nm by the intensity measured in the absence of rho-PE for each proportion of rho-PE to cou-PE. This fractional intensity was assumed to be the ratio of the quantum yield of cou-PE undergoing RET to its quantum yield in the absence of RET, Φ_{DA}/Φ_D, which equals 0.5 at an acceptor density equivalent to 1 acceptor in a circular area of $5\pi R_0^2$ (Estep and Thompson, 1979; Wolber and Hudson, 1979; Dewey and Hammes, 1980). Φ_{DA}/Φ_D is plotted as a function of rho-PE:cou-PE in Fig. 2 *C*. This parameter is reduced to 0.5 at a rho-PE mole fraction of 5.63×10^{-3}, which, at 0.6 nm^2 area/lipid, leads by the above relation to an experimentally determined R_0 of 3.211 ± 0.301 nm. Using 1.334 as the refractive index, n, and the other, experimentally determined parameters listed in Table I, we calculated estimates of R_0 as 3.060 ± 1.605 nm for $\kappa^2 = 0.35$ and as 3.548 ± 2.264 nm for $\kappa^2 = 0.85$. As these calculated estimates bracketed the experimentally measured value, we used R_0 = 3.211 nm to interpret the RET images.

RET Imaging of Vesicle-Planar Membrane Interactions by Video Microscopy

Fluorescent lipid vesicles used for RET with planar membranes. Large liposomes, 1–20 μm in diameter and labeled with cou-PE, were prepared as previously described (Kim and Martin, 1981; Niles and Cohen, 1987). The total lipid used in each vesicle preparation was 15.51 μmol, which consisted of 3.35 μmol PC, 3.35 μmol PE, 2.51 μmol PS, 7.5 μmol cholesterol, and 3.0 μmol triolein. Cou-PE was added to the lipid mixture to obtain the desired mole fraction of donor probe, which was either 1.0, 2.0, or 4.0 mol%. Vesicles were prepared fresh daily and stored on ice before use.

Fluorescent planar membranes. Planar membranes were formed across a circular orifice 160 μm diam in a 50-μm thin septum of black Teflon submerged in buffer solution, consisting of 120 mM NaCl, 10 mM HEPES, 3 mM $MgCl_2$, 1 mM EDTA, pH 7.4. Membranes were formed by brushing a solution of 50 mg/ml lipid in squalene across the hole (Needham and Haydon, 1983). Thinning was determined both optically by the formation of the Plateau-Gibbs border in bright-field transillumination and electrically by the growth of bilayer capacitance. Sometimes membranes were formed by spreading 5 μl of 10 mg/ml lipid in pentane at the air-water interface with the solution level below the squalene-coated orifice. Solution was then added to raise the lipid monolayers over the hole (Montal and Mueller, 1972). Both types of membranes produced identical results. The lipid composition of the membrane-forming solutions was 3:1 phospholipid:cholesterol (mole fraction) and the composition of the phospholipid portion was 2:2:1 PC:PE:PS. The mole fraction of the acceptor probe rho-PE was either 1.0, 2.0 or 4.0 mol% of the total phospholipid in the membrane-forming solution.

Planar membrane chamber. The septum in which the planar membrane was formed divided a Teflon chamber into two solution-filled compartments (Niles and Cohen, 1987). The front and back sides of the chamber were No. 1 cover slips to allow optical monitoring of the membrane. The chamber was mounted in a calibrated RET video microscope (Niles and Cohen, 1995). Donor-labeled vesicles were delivered to the planar membrane by pressure-ejection from an L-shaped micropipette in the *cis* compartment, as described (Niles and Cohen, 1987), while the membrane was viewed with the microscope through the *trans* compartment. The *cis* compartment was continually stirred by a Teflon-coated flea.

RET imaging video microscope. The donor coumarin in the vesicles was excited by epi-illumination with monochromatic 390 nm light. The emissions from both the coumarin and rhodamine probes were collected by the microscope objective (MPlan 25X/0.4 NA, 11 mm working distance, E. Leitz, Edison, NJ) and separated by a series of filters into coumarin- and rhodamine-originating components (Niles and Cohen, 1995). Emitted light with wavelengths <510 nm was directed to a KS1380 multichannel plane image intensifier (Videoscope International, Washington, DC) coupled to a CCD-72 camera (Dage-MTI, Inc., Michigan City, IN) to detect the donor fluorescence from cou-PE in the vesicles. Wavelengths >510 nm were directed to a KS1381 intensifier-CCD camera to observe the acceptor fluorescence image originating from the rho-PE in planar membrane. The donor and acceptor images were observed simultaneously and archived on tape using two video tape recorders. Time stamps written on each video frame were used to synchronize the two images. Tape records were transferred to optical disk for subsequent analysis with an image processor (Series 151, Imaging Technology, Inc., Woburn, MA).

RET ratio images. RET was analyzed by calculating the sensitization ratio $\Delta I_A/I_D$ (Eq. 3) at each pixel location. Each ratio image was computed from one image of donor coumarin fluorescence and two images of acceptor rhodamine fluorescence. One acceptor image was obtained simultaneously with the donor image in the presence of energy transfer. The second acceptor image was obtained at a time prior to RET and was used to remove acceptor fluorescence unrelated to RET from the first image. We converted the video brightnesses in each image, which corresponded to photometric intensities, into area-normalized energy fluxes (radiometric intensities) using calibration procedures that we have established for this video microscope—video luminance brightnesses were converted to irradiances by calibrating against a photodetector corrected for its own spectral response (Niles and Cohen, 1995). This enabled the sensitization ratios to be computed as energy ratios, allowing accurate intermembrane separation distances to be calculated.

We computed sensitization ratio images for each experiment by the following procedure. The donor image was selected after unbound vesicles ejected from the pipette were swept away by stirring. The coumarin emission intensity I_D was calculated by temporally averaging 4–32 frames of the donor image and subtracting a 32-frame average background brightness image, obtained before vesicle ejection. The averaged brightness of each pixel in the frame was transformed to the irradiance falling on the donor camera using its brightness-irradiance relation (Niles and Cohen, 1995). The total emission intensity of acceptor at each pixel I_A was determined from a temporal average of 32 frames of the rhodamine image starting at the same time as the first frame of the donor image, which was then converted using the acceptor camera brightness-irradiance relation. I_A contained acceptor emission sensitized by RET from coumarin, but it also

included rhodamine fluorescence due to direct excitation by the 390 nm illumination. To remove the background intensities, 32 frames of the rhodamine image of the planar membrane obtained before the ejection of vesicles were averaged and transformed to I_A^0. ΔI_A, the rhodamine emission intensity due to RET, was calculated as $I_A - I_A^0$. Before calculation of the sensitization ratio, the irradiances ΔI_A and I_D were divided by the spectral transfer factor of the respective emission pathway, listed in Table II, to convert them to radiances at the specimen plane (Niles and Cohen, 1995). As transmission of the coumarin emission through the acceptor pathway and rhodamine emission through the donor pathway were negligible, we corrected the coumarin and rhodamine intensities only with the spectral transfer coefficients of their respective pathways.

The sensitization ratio $\Delta I_A/I_D$ was computed for each pixel and then converted into the intermembrane separation distance at that location. Substitution of Eq. 4a into Eq. 3 yields the expression for $\Delta I_A/I_D$ as a function of the intermembrane separation distance a. Using $k_D^f = 1/\tau_D$, we applied the inverse formula

$$a = \left[\frac{(\pi/2)\,A_T}{\Delta I_A/I_D}\right]^{1/4} (R_0)^{3/2} \qquad (5)$$

to the sensitization ratio value at each pixel in the image to obtain a. The area density of rho-PE (A_T) was determined from the mole fraction of acceptor in the membrane forming solution.[1] The computed distances were then mapped to the brightness scale of [0,255] with 6 nm represented by 0 brightness units and 1 nm by 255, with unit increments in the linear greyscale denoting logarithmic decrements in distance.

Distributions of the fractional surface area of the vesicle in contact with the planar membrane. Distributions of the area of the vesicle in contact with the planar membrane were calculated as functions of intermembrane separation. For each intermembrane separation distance a, we determined the fractional area of the vesicle with a separation distance from the planar membrane $\leq a$. With each vesicle, we counted the number of pixels, N_D, in the donor coumarin image with brightnesses equal to or greater than a threshold brightness. We assumed that the donor image provided a hemispherical profile of the vesicle, so that the total surface area of the vesicle was 2 N_D a_p, where a_p is the area per pixel (0.2384 μm^2). We overlayed a boundary on the ratio image at the spatial location corresponding to the edge of the vesicle in the donor image, to ensure spatial coincidence of the ratio image pixels used to determine the area of contact and the particular vesicle. Because the true edge of a spherical vesicle was indeterminate in a discretely sampled 2-dimensional profile, the boundary in the ratio image was made three pixels wide extending away from the edge of the vesicle determined in the donor image. A brightness histogram of the pixels in the ratio image both within and directly under the vesicle boundary was constructed, yielding the histogram of intermembrane separation. To generate the distribution, we counted the number of pixels with intermembrane separations equal to or greater than each possible distance a, denoted as $N_A(a)$. The fraction of the vesicle's total surface area separated by a distance $\leq a$ from the planar membrane was calculated as $N_A(a)/2\,N_D$.

[1]We attempted to observe lateral separation of lipids into domains of similar curvature by bathing rhodamine-labeled planar membranes in 100 mM Ca^{2+} in the absence of vesicles and directly exciting the rho-PE. We expected phase domain formation to be accompanied by the formation of spatial regions of high and low fluorescence, because the rho-PE is anionic and might be expected to cosegregate into a region of anionic lipids by the formation of lateral cross-bridges by Ca^{2+}. This was not observed to occur; sterol may be azeotropic and prevent phase separation.

TABLE II

Spectral Transmission of Coumarin-PE and Rhodamine-PE Emission through the Donor and Acceptor Optical Pathways of the RET Microscope

	Probe emission	
Optical pathway	Coumarin-PE	Rhodamine-PE
Donor	0.05949	8.2×10^{-5}
Acceptor	7.31×10^{-4}	0.2623

The spectral transfer function for a given pathway i is $\int S_i(\lambda) f_j(\lambda)\,d\lambda$, where $S_i(\lambda)\,d\lambda$ is the spectral transfer coefficient for the i-th emission pathway over the wavelength range $[\lambda, \lambda + d\lambda]$ and $f_j(\lambda)\,d\lambda$ is the relative fluorescence of the j-th probe over the same wavelength range (Ludwig et al., 1992).

RESULTS

RET between Coumarin and Rhodamine

The fluorescence and RET properties of cou- and rho-PE in membranes viewed with the video RET microscope were the same as those determined by spectrofluorimetry of dye-containing liposomes. Excitation spectra of solvent-free planar membranes containing 2 mol% coumarin- or rho-PE (Fig. 3 *A*) were obtained from the fluorescence intensity measured at each excitation wavelength. This was the integral of the fluorescence emission intensity-spectral transfer function product over the passband of the microscope emission pathway. The excitation spectra of the probes in solvent-free planar membranes, measured with the microscope, were similar to the absorption spectra of the probes in detergent-dialysis liposomes, obtained fluorimetrically, including the decreased intensity of cou-PE relative to rho-PE. The RET characteristics of the probes in planar membranes also were the same as those obtained in liposomes. We compared $\Delta I_A/I_D$ measured spectrofluorimetrically for labeled detergent dialysis liposomes with those obtained in the RET microscope with planar membranes thinned from squalene solutions containing the same mole percentages of probes as the liposomes (see Fig. 3 *B*). The sensitization ratios of the liposomes (*open squares*) were greater than those of the planar membranes (*closed diamonds*) at the same proportion of labeled to unlabeled probe. This was because I_D values measured in the microscope were emission intensities integrated over the passband of the donor emission pathway of the microsope (see Table II), which were proportionally larger than the fluorimetric cou-PE intensities measured at a single wavelength for the liposomes. Both methods revealed self-

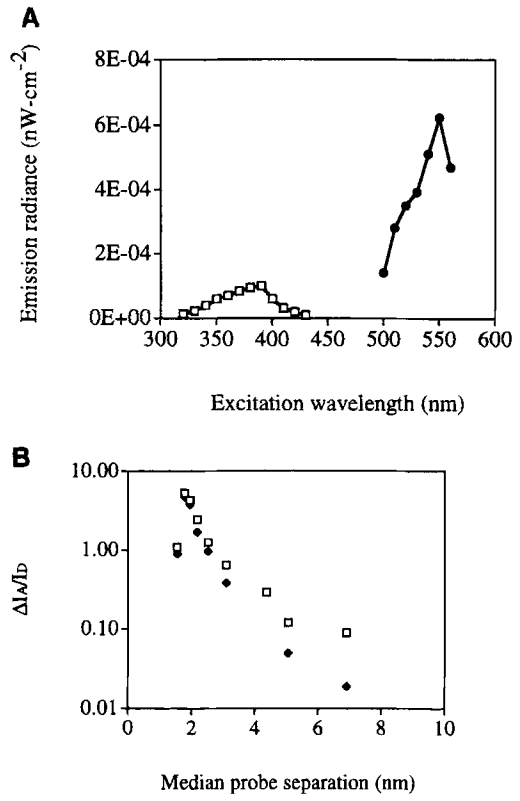

FIGURE 3. Fluorescence and RET properties of cou-PE and rho-PE in planar membranes measured by radiometric fluorescence microscopy (*open boxes*). (*A*) Excitation spectra of planar membranes labeled with cou-PE and rho-PE (*filled circles*). Planar membranes, thinned from phospholipid solutions in squalene, contained 1 mol% of either label and were bathed in solution containing 15 mM $CaCl_2$. The wavelength of the excitation epi-illumination light was swept with a monochromator through the range indicated on the abscissa. The cou-PE emission was recorded with an intensifier-CCD video camera at the donor emission port which received wavelengths <510 nm. The rho-PE emission was recorded with a second intensifier-CCD operated at higher gain at the acceptor port which received wavelengths >510 nm. The intensities indicated on the ordinate are 32-frame averaged video brightnesses converted to radiances using the spectral transfer functions of the emission pathways of the microscope and the irradiance-brightness relations of the cameras (Niles and Cohen, 1995). (*B*) Sensitization ratios of rho-PE fluorescence intensity to cou-PE intensity for liposomes (*open squares*) and planar membranes (*filled diamonds*). Detergent-dialysis liposomes contained 1:1 mole fraction ratios of cou- to rho-PE. The mole ratio of each probe relative to unlabeled lipid was 0.005, 0.075, 0.1, 0.15, 0.2, 0.5, 1.0, 2.0, or 4.0 mol%. Sensitization ratios ($\Delta I_A/I_D$) for each probe ratio were calculated from emission spectra (excitation at 390 nm) by dividing the emission intensity at 570 nm by the intensity at 440 nm. Background excitation of rho-PE at 390 nm was determined with a second preparation of liposomes containing only rho-PE at the same mole percentage. The background emission intensity at 570 nm was subtracted from the intensity obtained with colabeled liposomes to calculate ΔI_A. The planar membranes were formed from lipid mixtures in squalene identical to those used to make the labeled liposomes. The solution bathing the membranes contained 20 mM $CaCl_2$. The coumarin was excited at 390 nm, and

quenching of rho-PE fluorescence at 4 mol%, which decreased the sensitization ratios in Fig. 3 *B*. The important feature is the identical variation of the sensitization ratio with probe separation over the 2 to 6 nm distance range, where we measured vesicle-planar membrane separations. Thus, the RET charateristics measured fluorimetrically with liposomes are applicable to microscopic measurements of vesicle interactions with planar membranes.

Interactions between Vesicles and Planar Lipid Membranes

Delivery of vesicles to the planar membrane. We pressure-ejected large vesicles at the planar membrane from a pipette located in the *cis* compartment that was brought close to the membrane. Vesicles were very bright in the field of view and so the donor camera was operated at an intensifier gain ranging from 0.67 to 3.5% of maximum. Some of the ejected vesicles adhered to the planar membrane, when millimolar concentrations of Ca^{2+} were present in the *cis* solution. A 3-ms duration ejection typically released 20–50 vesicles, and 5–20 of these vesicles encountered the planar membrane in that they rapidly decelerated and appeared in focus at a single plane. Out of these vesicles, 0–10 vesicles adhered, with the actual number bound dependent on the calcium concentration. The adsorbed vesicles were easily distinguished from their unbound counterparts, as the latter were removed from the field of the view by the continuous stirring of the *cis* solution, often moving out of focus before leaving the field of view. The bound vesicles, in contrast, remained in focus at the planar membrane, sometimes moving slightly under the force of the continual sweep of the stirred buffer (Niles and Cohen, 1987, 1991). In the absence of any osmotic gradients causing swelling, the bound vesicles were stable and did not fuse with the planar membrane, as soluble intravesicular fluorescent dyes were not released (Niles and Cohen, 1987).

Lack of intermembrane transfer of probes. By measuring RET, we established that fluorescent lipids in cou-PE and rho-PE colabeled liposomes (4:1 PC:PS) did not spon-

the video brightnesses recorded by the two cameras were transformed to radiances at the specimen plane as described in Materials and Methods. Ratios were calculated after subtraction of the background I_A^0 from the radiance measured with the acceptor camera. I_A^0 was measured at 390 nm excitation of a planar membrane containing only rho-PE (no couPE) at the same mole percentage of acceptor as in the membrane RET mixture. The abscissa denotes the median radial separation between probes calculated for each mole percentage as previously described (Niles and Cohen, 1995). The $\Delta I_A/I_D$ of the planar membranes are slightly below those obtained with liposomes as described in Results. The variation of $\Delta I_A/I_D$ with median probe separation is the same for both liposomes and planar membranes.

taneously transfer to unlabeled liposomes over a period of 3 h (data not shown). This result agrees with previous observations that neither rho-PE nor an acyl-chain-labeled analogue of cou-PE exchange between liposomes over this time (Hoekstra et al., 1984; Silvius et al., 1987).

The intensifier-CCD cameras of the RET microscope are sensitive to the low intensities emitted by a small number of probes and were capable of detecting dye transfer, if any, between the vesicular and planar membranes in the region of contact (Niles and Cohen, 1995). We ejected large vesicles containing 5 mol% cou-PE at unlabeled planar membranes bathed in 20 mM Ca^{2+}. We assessed redistribution of the cou-PE from the bound vesicles by looking for changes in their brightness distributions. We assumed that cou-PE transferred to the planar membrane would laterally diffuse and produce an image increased in diameter and diminished in intensity relative to the initial vesicle profile.

With planar membranes thinned from squalene, which are effectively solvent-free (Needham and Haydon, 1983), cou-PE rarely migrated from the vesicular to the planar membranes. The stability of cou-PE in vesicles is shown in Fig. 4 *A*. The top panel shows images of two vesicles ~3 s after encountering and binding to a planar membrane thinned from squalene. The same two vesicles 10 s later are shown in the bottom panel. The two images of each vesicle were nearly identical at both times with no change in their brightness distributions. In 119 vesicles bound to squalene-thinned films, lateral spread of cou-PE fluorescence was detected in only 4 vesicles (<3%). Therefore, hemifusion was a rare event.

With planar membranes thinned from decane, however, migration of cou-PE from the vesicular to planar membranes was detected more frequently, in 9 out of 53 vesicles observed (~16%). Two examples are shown in Fig. 4 *B*, in which the bound vesicles ~3 s after encountering the planar membrane are shown in the top panel and the same vesicles 10 s later are shown in the bottom panel. For both vesicles, the dye spread laterally from its initial distribution during the 10-s period, which increased the apparent vesicle areas and diminished their brightnesses. The extent of dye redistribution was not the same for the two vesicles, although each vesicle's brightness integrated over the area of each profile was the same before and after dye spread. The extents of dye redistribution were consistent with diffusion in decane films. The brightness profiles were relatively stationary after the initial spread, however, suggesting that dye spread stops. This is consistent with the melding of the facing monolayers of the vesicle and planar membranes and the formation of a microlens with an aqueous core in the decane film, which limits the spread of the lipid dye confined by the vesicle and hemifusion diaphragm (Perin and MacDonald, 1989). We observed no transfer of rho-PE from vesicles to solvent-free membranes in separate experiments.

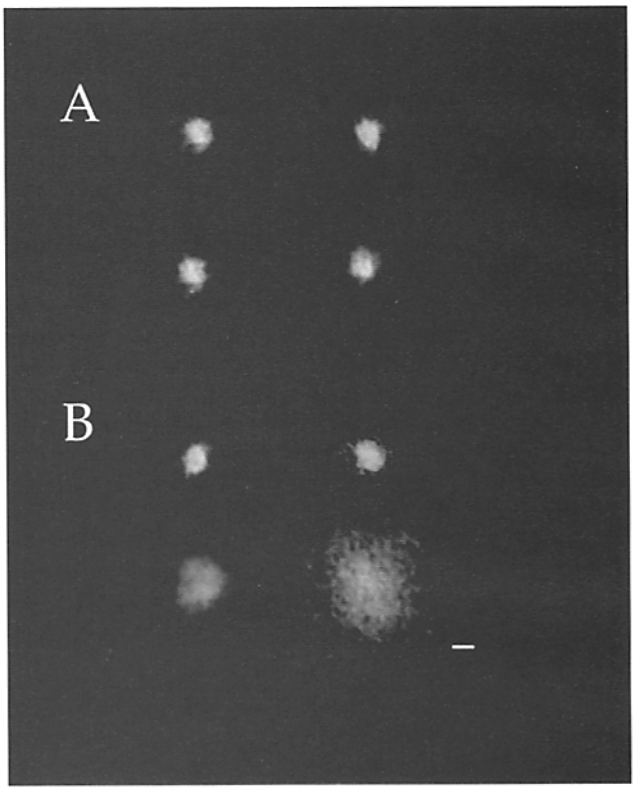

FIGURE 4. Probe does not migrate to solvent-free membranes but does to solvent-containing membranes. Large vesicles labeled with 5 mol% cou-PE were ejected at unlabeled planar membranes bathed in buffer containing 20 mM $CaCl_2$. Each vesicle image was recorded with the donor camera operated at the intensifier gain set at 5% of maximum. In both *A* and *B*, the top two images are eight-frame averages of different vesicles at ~3 s after contacting the planar membrane, as determined by their remaining within a fixed plane of focus. The bottom two images are the same vesicles 10 s later. (*A*) Solvent-free membranes thinned from squalene. The dye remained confined to the vesicle and did not migrate to the planar membrane, as the profiles of each vesicle at the two epochs are essentially identical. The low intensity wisps extending away from the vesicle profiles were extraneous background fluorescence unrelated to the vesicles. Less than 3% of labeled vesicles lost dye to solvent-free planar membranes. (*B*) Solvent-containing planar membranes thinned from decane. For both vesicles, after 10 s, sufficient dye had migrated to the planar membrane and diffused from the region of contact so that each vesicle image occupied a larger area and was decreased in intensity at each spatial location. Scale bar, 5 μm.

The Region of Vesicle-Planar Membrane Contact

Calibration of intermembrane separation in acceptor sensitization ratio images. To study the localized interactions between the membranes in the region of contact, we

ejected large vesicles labeled with 1–4 mol% cou-PE at planar membranes labeled with 1–4 mol% rho-PE.

To obtain intermembrane separation distances from the ratio images, we assumed that the donor and acceptor probes were confined to distinct planes separated by a constant distance within the area of each image pixel. Deviations of the actual geometry from the assumed arrangement produced errors in the determined intermembrane separation. To minimize this source of error, large dye concentrations were used to pack enough probes at each location in the image to validate the plane–plane interaction assumption within each pixel. The high probe densities produced self-quenching of the probe fluorescences, primarily of rho-PE, at the densities used. This decreased the intensity of the sensitized acceptor fluorescence and lowered the effective R_0 estimated from the diminution of donor fluorescence in liposomes (Ludwig et al., 1992).

Errors in the distance measurements. The effect of R_0 on the probe separation producing each k_t is shown in Fig. 5 *A*, in which the k_t calculated with Eq. 4 *A* is plotted as a function of separation distance between the planes, *a*, for R_0 of 2.8 (*boxes*) and 3.6 nm (*diamonds*), a range that spans the possible values of R_0 in our experiments. At a fixed value of k_t, the difference in the distances predicted using the two different values of R_0 ranges from <0.5 nm at $a \leq 1.0$ nm to ~1.5 nm at $a = 6.0$ nm, because the separation distance estimated with the sensitization ratio varies with the 3/2 power of R_0 (Eq. 5). For the R_0 that we used, 3.21 nm, midway in the range, the error was <0.5 nm at distances ≥1.0 nm, and errors in our estimate of R_0 due to self-quenching of the acceptor fluorescence produced relatively small errors in the estimated distances. The calibration curve (Eq. 5), used to determine *a* from $\Delta I_A/I_D$, is shown in Fig. 5 *B*. Because the ratios at $a < 1.0$ nm are very large and, hence, very sensitive to errors due to acceptor self-quenching, 1.0 nm is the closest separation distance calibrated in the ratio images. In addition, the probes are assumed to interact as dipoles in Förster theory, and this assumption breaks down at separations close to the dimensions of the fluorophores (Kuhn, 1970).

The Region of Adhesion between Vesicles and Planar Membranes—Ca^{2+} Dependence

General observations. When cou-PE labeled vesicles were ejected at rho-PE labeled membranes, sensitization of rho-PE fluorescence by RET was observed when the *cis* solution contained Ca^{2+}. Representative images of two

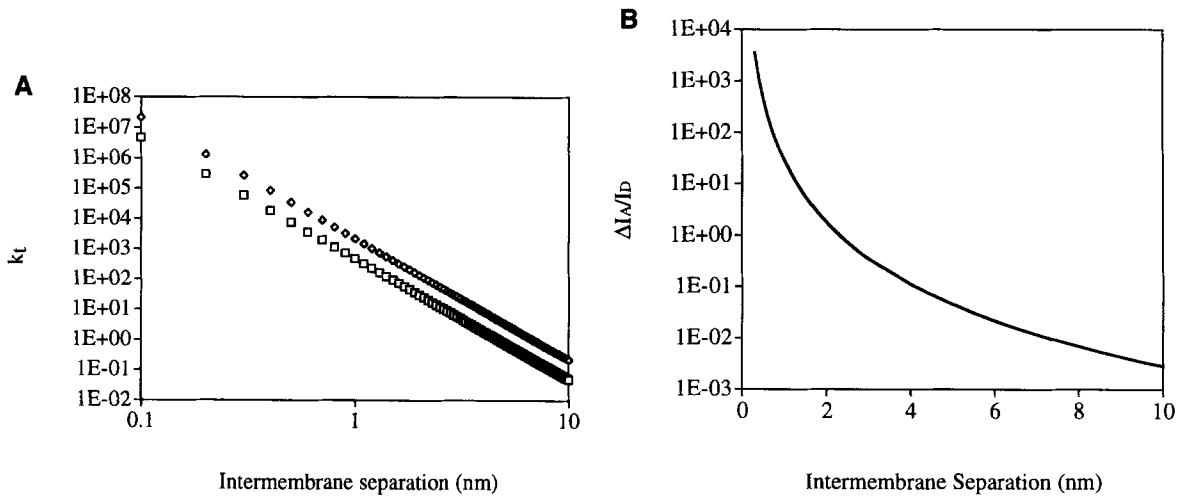

FIGURE 5. Calibration of the sensitization ratio as intermembrane separation distances. The donor and acceptor probes were assumed to be located in separate parallel planes. (*A*) The effect of variation in R_0 on the RET rate constant k_t. The RET rate constant is shown plotted as function of intermembrane separation distance, *a*, predicted by Eq. 4a for limits of the critical distance R_0 that span the range calculated and measured for the cou-PE/rho-PE dye pair. (*Open boxes*) $R_0 = 2.8$ nm; (*open diamonds*) $R_0 = 3.6$ nm. At any fixed *a*, the two values of k_t differ by a factor of 4.5, due to the variation of k_t with the sixth power of R_0. However, the separation distances change by a factor of only 1.46 at a fixed k_t over this range of R_0 because *a* varies as the 3/2 power of R_0. For intermembrane separations between 1/3 and 3 times R_0, the error in *a* is small. We used the value of $R_0 = 3.2$ nm determined experimentally from liposomes under conditions very similar to those in the vesicle-planar membrane binding experiments. Errors in distance due to uncertainties in R_0 were at most ~50%. (*B*) The calibration of the sensitization ratio with intermembrane separation distance. Eq. 5 was used to determine the variation of $\Delta I_A/I_D$ with *a*. The curve shown was calculated with $A_T = 1.67 \times 10^{12} cm^{-2}$, corresponding to 1.0 mol% acceptor. This curve was used to convert the experimentally measured ratios in vesicle-planar membrane binding experiments to intermembrane separation distances. Although the model used to determine Eq. 4 assumed that the planes in which the probes were confined were infinite in area, the difference introduced by truncating the limits of integration was very small. For a square pixel 488 nm in length on a side, at a constant intermembrane separation distance of 6 nm, the limits of integration are decreased from 90 to 89.2°.

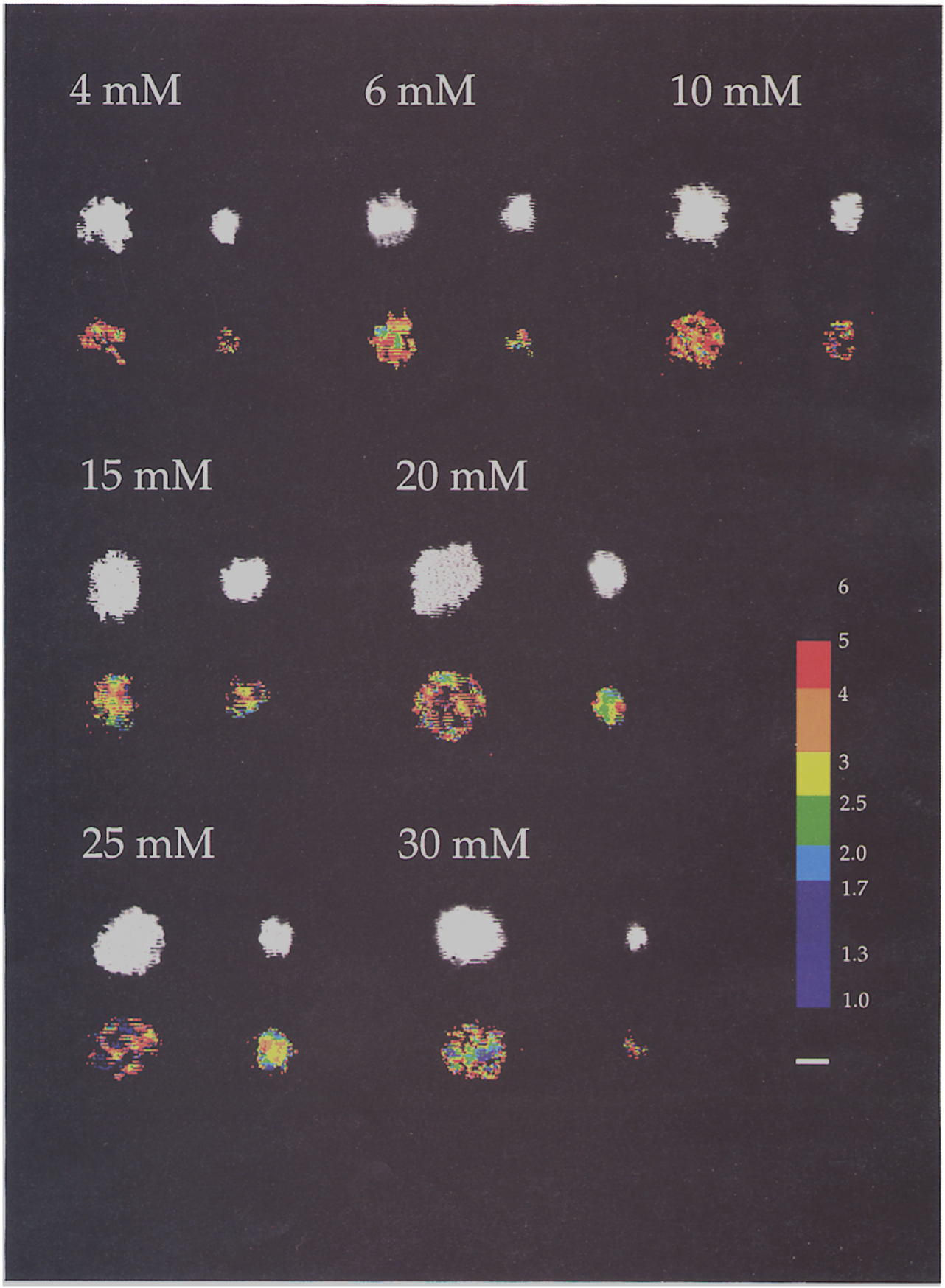
4 mM
6 mM
10 mM
15 mM
20 mM
25 mM
30 mM
6
5
4
3
2.5
2.0
1.7
1.3
1.0

vesicles obtained at each [Ca^{2+}] are shown in Fig. 6. The upper panel in each row is the cou-PE fluorescence image of the bound vesicle in contact with the planar membrane and the lower panel is the sensitization ratio image computed for the same vesicle with the intermembrane separation distance encoded as a pseudocolored brightness. In all cases, sensitization of acceptor fluorescence was spatially localized within the perimeter defined by the edge of the vesicle.

The character of the ratio image was greatly influenced by [Ca^{2+}]. In the nominal absence of Ca^{2+} in the solution of the *cis* compartment, very little if any sensitization of rho-PE fluorescence was observed (not shown). The solution in the zero Ca^{2+} experiments contained no added Ca^{2+}, but did contain ~2 mM free Mg^{2+} (a small amount of divalent cation was necessary for stability of the planar membrane). The very small amounts of RET rarely detected at 0 Ca^{2+} must have been due to adhesion mediated by the free Mg^{2+}. This is consistent with the absence of vesicular binding to planar membranes under these conditions (Niles and Eisenberg, 1985; Niles and Cohen, 1987), and verifies that the lack of membrane fusion in the presence of an osmotic gradient but zero Ca^{2+} arises from the inability of the vesicles to stably contact the planar membrane (Cohen et al., 1980; Akabas et al., 1984).

At increased Ca^{2+}, the fluorescence of the rho-PE in the planar membrane was sensitized by RET due to the encroachment of the cou-PE localized to the vesicular membrane. Because RET between the headgroup-located probes occurred appreciably only at membrane separations <10 nm, we regarded the area of rhodamine fluorescence sensitization to be coincident with the adhesion interaction between vesicular and planar membranes and the formation of a stable region of close apposition or contact. We adopted a minimum distance of 6 nm as an arbitrary intermembrane separation that defined contact. Although the RET calibration was sensitive to distances of 35 nm, we rarely detected intermembrane separations >6 nm.

The contact regions were stable. Lowering [Ca^{2+}] by the addition of excess EDTA to the *cis* solution after vesicular binding did not cause the vesicles to detach or the contact regions to change for up to 10 min (the longest time observed) so we assumed the vesicle-planar membrane reached equilibrium. Thus, the [Ca^{2+}] necessary to obtain stable adhesion was unrelated to the [Ca^{2+}] necessary to maintain it. At 4 and 6 mM, we observed that a few vesicles with separation distances ≥4 nm from the planar membrane occasionally detached after a few seconds or minutes of contact. Their ratio image profiles did not change as long as they were attached.

The most striking feature of the region of vesicle-planar membrane contact was its variability in area and in the distances between the membranes. Some contact regions were highly variegated in shape, to the extent of forming discontinuous zones on the same vesicle, while others were continuous with relatively smooth edges. The distances between the membranes were highly variable. Areas of relatively smooth change in intermembrane separation were abruptly interrupted by punctate zones where the membranes were very closely applied. This variation of distance within the contact region was a common feature. Because tension (Needham and Haydon, 1983) damps the undulations of planar membranes (Evans and Ipsen, 1991; Lipowsky, 1991), this indicated that the membranes of the unpressurized vesicles were flexible and capable of undulation prior to adhesion.

The surface area of the vesicle in contact with the planar membrane. The region of contact established by membrane-membrane interaction in the presence of Ca^{2+} varied in a multiphasic way with concentration. As [Ca^{2+}] was increased from 0 to 15 mM, the region of contact became larger in area, while at concentrations >15 mM, the membranes came closer together. The distributions of the intermembrane separation distances in the region of contact at different [Ca^{2+}] illustrate this on a quantitative basis in Fig. 7 *A*. The distance distributions show the fraction of the vesicle surface area in contact with the planar membrane at distances less than or equal to the indicated intermembrane separation. The errors associated with these distributions were small, the coefficient of variation at each distance of intermembrane separation was <4%, so differences between these curves are meaningful.

At concentrations ≤15 mM, increased Ca^{2+} brought a greater proportion of each vesicle's area into apposi-

FIGURE 6. Images of coumarin-PE labeled vesicles adhered to rhodamine-PE labeled planar membranes at different [Ca^{2+}]. Below the text denoting each [Ca^{2+}], the top two images are 16-frame brightness averages of vesicles labeled with 2 mol% coumarin-PE obtained with the donor camera operated at an intensifier gain of 3.5% of maximum. Two vesicles, one relatively large in diameter and the other relatively small, are shown for each [Ca^{2+}]. The brightnesses are those directly recorded by the camera and are not transformed to radiances. The image below each vesicle is the sensitization ratio image for the same vesicle calculated as described in Materials and Methods. The sensitization ratio at each pixel was converted to intermembrane separation distance with Eq. 5. The resulting intermembrane separation distances were encoded as pseudocolor brightnesses shown in the scale at the lower right. At [Ca^{2+}] <15 mM, the area of the contact region increased with [Ca^{2+}]. At larger [Ca^{2+}], the total area of the contact region decreased, but the proportion of membrane with bilayer separations <2 nm increased. Scale bar, 5 μm.

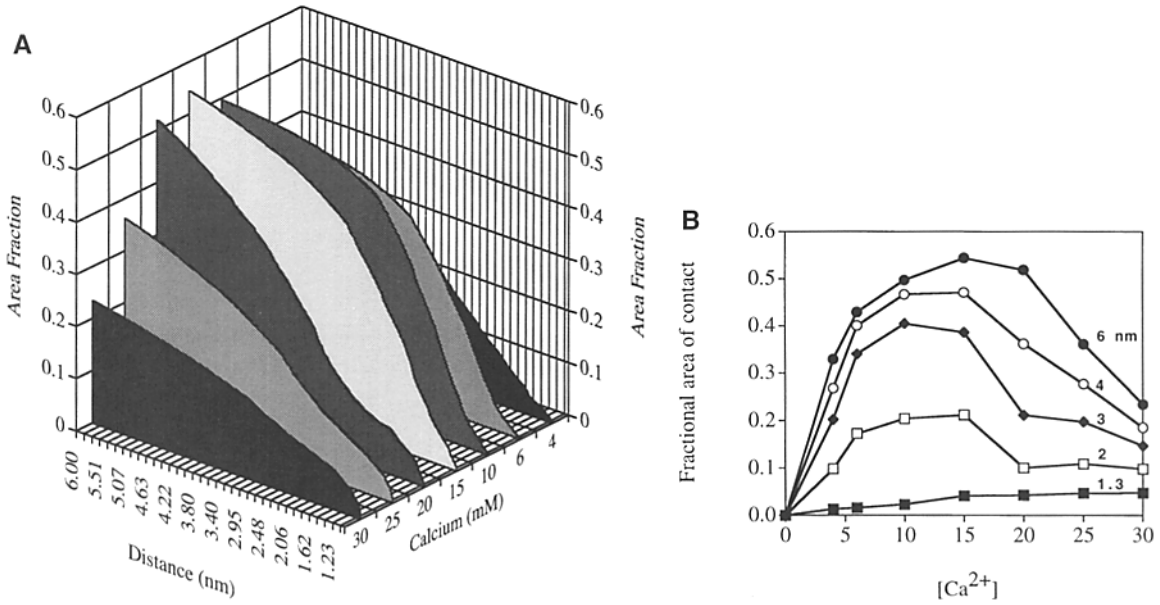

FIGURE 7. Intermembrane separations in the region of vesicle-planar membrane contact. (*A*) Distributions of intermembrane separation distance in the contact region at $[Ca^{2+}]$ ranging from 4 to 30 mM as a three-dimensional area plot. Area distributions of the contact region at each intermembrane separation distance were calculated for each vesicle as described in Methods and Materials and Results. At each $[Ca^{2+}]$, the distribution values at each intermembrane separation were averaged for all vesicles. The ordinate denotes the fractional surface area of the vesicle membrane located from the planar membrane at distances less than or equal to the intermembrane separation distance indicated on the distance abscissa. The number of vesicles used to determine the average area in contact with the planar membrane at each $[Ca^{2+}]$: 4 mM, 121; 6 mM, 130; 10 mM, 146; 15 mM, 102; 20 mM, 71; 25 mM, 48; 30 mM, 126. The coefficient of variation in the distributional area at each intermembrane separation was <4% for all $[Ca^{2+}]$. (*B*) The area of contact at intermembrane separation distances ≤6 (*filled circles*), 4 (*open circles*), 3 (*filled diamonds*), 2 (*open boxes*), and 1.3 nm (*filled boxes*) as functions of $[Ca^{2+}]$. The distributional areas at these separation distances in *A* are replotted against $[Ca^{2+}]$. The intermembrane separation distance is indicated above each plot. The area of contact at separations ≤1.3 nm was increased with $[Ca^{2+}]$, although the total area of the vesicular membrane in the contact regions was decreased at high $[Ca^{2+}]$.

tion with the planar membrane. This is seen using 6 (*filled circles*), 4 (*open circles*), 3 (*filled diamonds*), and 2 nm (*open boxes*) separation distances as criteria and plotting these values of the fractional area of contact as a function of $[Ca^{2+}]$ (Fig. 7 *B*). This interaction was most likely due to electrostatic screening of the negatively charged membranes by the divalent cation, rather than by specific binding of Ca^{2+} to the anionic headgroups and formation of $Ca(PS)_2$ cross-bridges between facing monolayers of the apposed membranes (Portis et al., 1979). Very little of the contact area at these $[Ca^{2+}]$ was in regions with <2 nm intermembrane separation, which would be expected for cross-bridge formation. By 15 mM, the fractional area of contact at 6 nm separation increased to 54%, suggesting that the adhesion was sufficiently attractive as to induce curvature in the planar membrane, enabling it to cover more than half of the vesicle surface area (Akabas et al., 1984).

Between 15 and 20 mM $[Ca^{2+}]$, the nature of the adhesive interaction between the membranes was changed. Further increases in $[Ca^{2+}]$ no longer increased the total amount of the vesicle membrane brought close to the planar membrane, particularly at 2 and 3 nm criterion separations (Fig. 7 *B*). In fact, the area of the contact region was smaller than at lower concentrations for the 4 and 6 nm distances. For example, at 30 mM Ca^{2+}, the fractional area of contact within 6 nm was <25% of the vesicle surface area. Instead, the intermembrane separation distance was decreased; the membranes moved closer together. This is seen by adopting 1.3 nm as the criterion distance of separation defining contact (*filled boxes*, Fig. 7 *B*). The area of the region of close contact continually increased with $[Ca^{2+}]$. This relation was similar to the number of vesicles that attach to the planar membrane as a function of $[Ca^{2+}]$ (Niles and Cohen, 1987). The decrease in the total area of contact at higher $[Ca^{2+}]$ was consistent with divalent cation binding to anionic headgroups on each individual membrane, reversing the sign of the surface potential, and causing the two membranes to repel one another instead of cross-bridging the two membranes. The zeta potentials of liposomes containing 20% PS in 100 mM NaCl are known to reverse sign when the bulk $[Ca^{2+}]$ is

in the range of 12 to 17 mM (McLaughlin et al., 1981). The increase in the proportion of the region of contact occupied by close intermembrane separation distances did suggest, however, that cross-bridge formation had occurred at discrete sites.

Punctate attachment sites between membranes. The close interaction between vesicular and planar membranes was characterized by small, punctate regions where the membranes were pulled to separations <2.0 nm. These punctate zones were surrounded by regions where the intermembrane separation was greater. They sometimes appeared in ratio images as single pixels of large intensity embedded in darker regions. We have termed these regions "punctate attachment sites." As seen in Fig. 6, at least a few of these punctate attachment sites were present in the region of contact at nearly all $[Ca^{2+}]$. As $[Ca^{2+}]$ was increased above 15 mM, the density of the punctate attachments increased, and the sites represented a larger proportion of the region of contact (Fig. 7 *A*).

We examined the spatial relations between the punctate attachment sites in the contact regions to determine whether they were distributed randomly or were regularly spaced. Regular spacing might indicate the development of long-range order in membrane structure within the contact region (reminiscent of a thermodynamic phase transition) that could be due to the formation of lipid structures preceding membrane fusion. The presence of spatial order was assessed by calculating the two-dimensional autocorrelation function of each contact region's ratio image (Russ, 1992). For a pair of correlation lengths (ξ,η), the correlation amplitude is $c(\xi,\eta) = \int\int b(x,y)\ b(x+\xi,y+\eta)\ dx\ dy$, where $b(x,y)$ is the brightness of the pixel in the ratio image at location (x,y). We calculated the correlation amplitudes for each ratio image as $c(\xi,\eta) = \int\int \mid H(u,v) \mid^2 e^{2\pi i(ux+vy)}\ du\ dv$, where $H(u,v)$ was the two-dimensional Fourier transform of the ratio image, $H(u,v) = \int\int b(x,y)e^{-2\pi i(ux+vy)}\ dx\ dy$. For each $[Ca^{2+}]$, $c(\xi,\eta)$ was averaged over all the contact regions for each pair of spatial correlation lengths. The logarithms of the average correlation amplitudes were scaled to a 256 unit brightness range. The resulting average two-dimensional autocorrelation images are shown for each Ca^{2+} concentration in Fig. 8 *A*.

The autocorrelation images were dominated by the pattern of punctate attachment sites in the region of contact. Nonzero amplitudes occurred at discrete correlation length pairs (ξ,η), which were repetitions of the fundamental pair (3,1) in a sparse tesselation pattern (Russ, 1992). All points in each correlation image were located at positions $(3m, 1n)$, where the repetition index m was drawn from the range of integers $\{1, N/3\}$, where N is the length (or width) of the contact area images used in the correlation calculation, and n was drawn from $\{1,N\}$. Because $m = n$ in the patterns we obtained, all points fell along discontinuous lines (runs) oriented at the same angle. While its physical basis is uncertain, the pattern indicated order in the region of contact. A random arrangement of intensities would

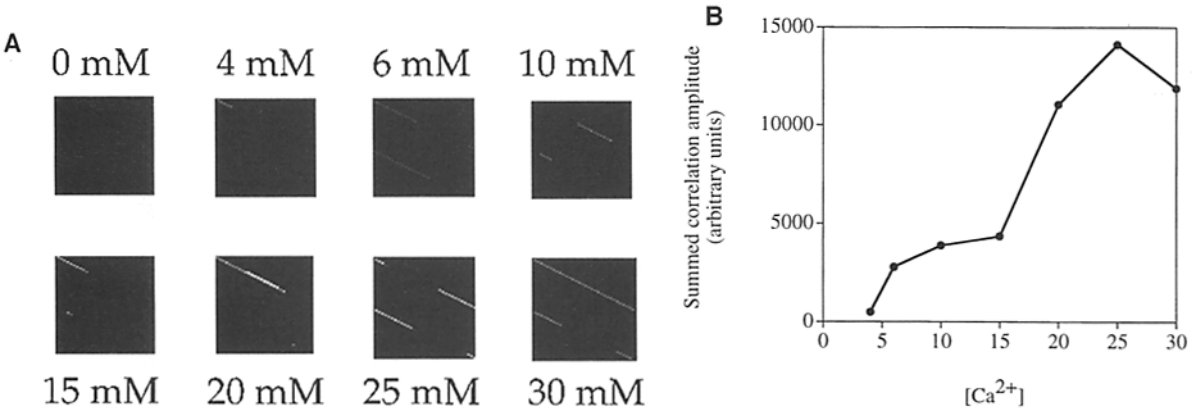

FIGURE 8. (*A*) Two-dimensional autocorrelation images of contact regions as a function of $[Ca^{2+}]$. Two-dimensional correlation functions were calculated as described in Results. Each panel is the averaged amplitude at each pair of correlation lengths for the regions of contact obtained at the indicated Ca^{2+} concentration. The correlation patterns were mapped to a fixed grid of 64 × 64 pixels, because the majority of ratio images were 64 × 64 pixels in size = 2^{12} pixels. However, we included all contact regions in the correlation calculations, some of which were 128 × 64 and 64 × 128 pixels in size (these were folded into the 64 × 64 grid). The amplitudes were logarithmically encoded as brightnesses, with the 0 level arbitrarily set to a correlation amplitude of 10^6, because this was the background amplitude uniformly distributed among all pairs of correlation lengths at $[Ca^{2+}] > 0$. The 255 level was set to 10^9. The nonzero amplitudes occur at discrete correlation length pairs arranged along lines (runs), indicating a set of fixed phase relations in the regions of contact. The breaks in the runs and the vertical shifting of run segments resulted from the inclusion of nonsquare ratio images in the correlation calculation. (*B*) Order parameter as a function of $[Ca^{2+}]$ in the regions of contact. The order parameter amplitude at each $[Ca^{2+}]$ was calculated as described in Results. The increased strength of the two-dimensional correlation at higher $[Ca^{2+}]$ indicated that as the number of punctate attachment sites was increased, they were arranged in the same pattern observed at lower $[Ca^{2+}]$.

produce a uniformly grey correlation image, with all length pairs having equal intensity as the fundamental length pair would be (1,1) and m and n would completely cover the range $\{1,N\}$ in all pairwise combinations. Random components in our correlation images were less than the threshold criterion established in the logarithmic scaling. The nonzero amplitudes originated from the punctate attachment sites. Binary masking of the ratio images, so that only pixels representing intermembrane separations $\leq$2 nm had brightnesses of 255 (with all other separations set to a brightness of 0), produced autocorrelation images similar to those of Fig. 8 *A*. Thus, regions with intermembrane separations >2 nm were only weakly correlated and occurred independently of each other, and the regions of the area of contact with separations $\leq$2 nm comprised the most strongly spatially correlated parts of the ratio images. The patterns indicated that occurrence of a punctate attachment site at one location restricted the places at which subsequent sites could be formed so that the arrangement of punctate attachment sites in the region of contact was regular and not disordered.

As the punctate attachment sites became more frequent at increased $[Ca^{2+}]$, their arrangement was a repetition of the closely spaced pattern seen at lower $[Ca^{2+}]$. This is seen qualitatively in Fig. 8 *A* by the increased length of the runs at progressively higher $[Ca^{2+}]$, in which the repetition indices increased without a change in the fundamental length pair. In addition, the total correlation amplitude increased with $[Ca^{2+}]$. We calculated an order parameter as

$$\sum_{\xi,\eta} c(\xi,\eta)$$

by summing the correlation amplitudes over all correlation lengths at each $[Ca^{2+}]$. These order parameters are plotted as a function of $[Ca^{2+}]$ in Fig. 8 *B*. The increased order parameter at higher $[Ca^{2+}]$ indicated that the total correlation amplitude was increased as the number of punctate attachment sites in the contact region increased, and the short-range spatial order was preserved in the long-range pattern. Therefore, vesicle membrane in the region of contact is more structurally ordered than in free, unattached locations.

Membrane curvature in the region of contact. The pattern of variation of intermembrane separation within the contact area, in which the separation was small in one location, greater in adjacent locations, and then smaller in surrounding locations, suggested that the membranes within the region of contact were under a bending or curvature stress. This would be the case if the local curvatures in the region of contact were different from the intrinsic curvatures of the constituent lipid molecules (Helfrich, 1973). Lipids within the region of contact could have phase separated into different microdomains, decreasing the local bending energy. We determined the magnitudes of the curvatures within each region of contact by calculating the average and maximum changes in intermembrane separation distance between each pixel and its immediate neighbors. To quantify the apparent undulatory pattern of intermembrane separation, we computed the absolute values of the differences in intermembrane separation between each pixel and its eight surrounding neighbors. Pixels at the edges of the contact regions were compared only with other edge pixels and the adjacent interior pixels. The average change in intermembrane separation at each pixel was calculated as the arithmetic mean value of the 8 (or fewer) differences, and the largest difference between each pixel and its neighbors was tallied as the maximum change in separation. These averages and maxima were accumulated as distributions (Fig. 9, *A* and *B*) and normalized by the total number of pixels in all the regions of contact studied at each $[Ca^{2+}]$. In other words, the ordinate denoted the probability that the average (Fig. 9 *A*) or maximum (Fig. 9 *B*) intermembrane separation changed by at least the distance indicated on the abscissa on traversing a lateral distance of one pixel width, 488 nm.

The average and maximum pixel-to-pixel change in intermembrane separation was increased at greater $[Ca^{2+}]$. Quantitative interpretation of the change in separation distance as a curvature energy requires assuming the location of a neutral reference plane between the membranes and apportioning the curvatures between the two membranes (Siegel, 1993). Nonetheless, even without such an assumption, the distributions in Fig. 9, *A* and *B*, reveal that the the pixel-to-pixel change in intermembrane separation increases with $[Ca^{2+}]$. Between 4 and 15 mM $[Ca^{2+}]$, average pixel-to-pixel changes in intermembrane separation were confined to less than 3 nm, and at 30 mM, the average change was <4 nm (Fig. 9 *A*). Therefore, the average curvature free energies in the region of contact were relatively small, because the changes in membrane separation were relatively gradual with lateral distance, on average. The distributions of maximum change in intermembrane separation, however, revealed that a small but significant proportion of the region of contact was thrown into relatively large folds on the spatial frequency scale determined by the pixel width. At $[Ca^{2+}]$ >10 mM, the fraction of the region of contact with maximum pixel-to-pixel changes in membrane separation >4 nm was between 15 and 25%; the exact proportion depended on the $[Ca^{2+}]$ (Fig. 9 *B*). The partition of a relatively large proportion ($\sim$10%) of the contact area into discrete punctate attachment sites distributed across the face of the vesicle (Fig. 7, *A* and *B*) was consistent with the relatively large pixel-to-pixel change in separation. At $[Ca^{2+}]$ <15 mM, where the presence of

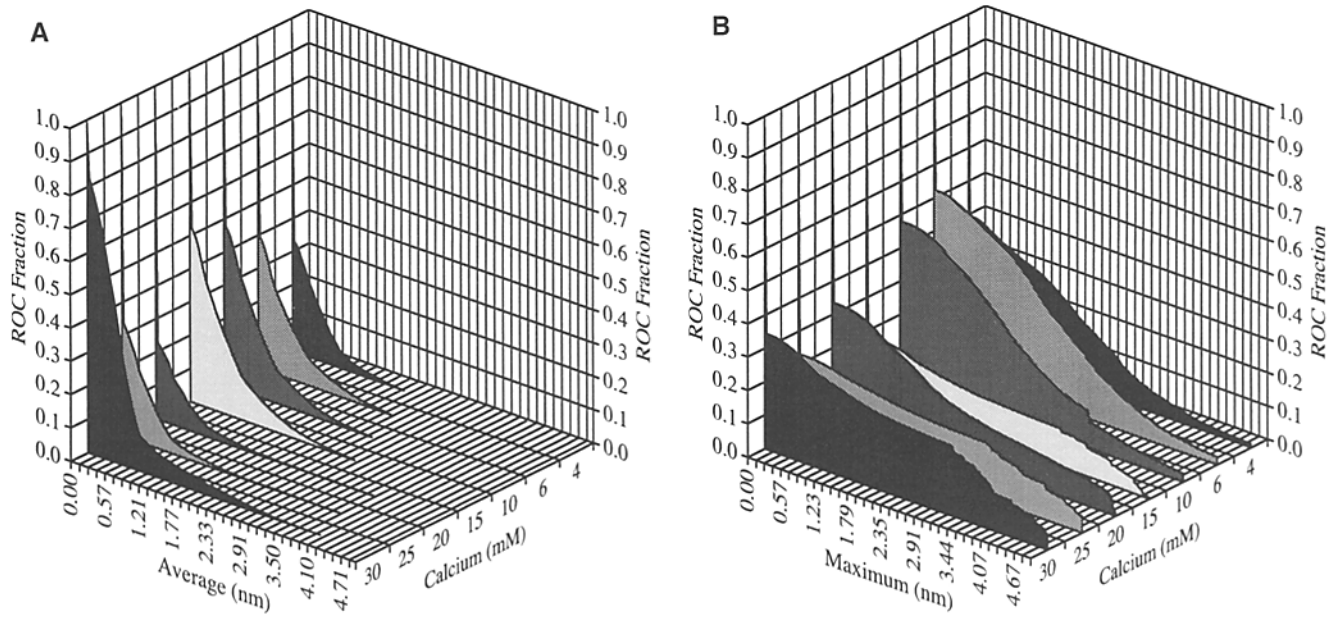

FIGURE 9. Pattern of membrane curvature in the region of contact (ROC) as a function of $[Ca^{2+}]$. The curvature pattern of intermembrane separation distances was characterized as the change in intermembrane separation between adjacent pixels. (*A*) The changes in intermembrane separation between each pixel and all of its adjacent pixels in the region of contact were averaged. (*B*) For each pixel, the maximum change in intermembrane separation distance between it and its adjacent neighbors was selected. The ordinate shows the proportion of pixels in the ROC with changes in separation ≥ the value indicated on the abscissa. The change in intermembrane separation increased with $[Ca^{2+}]$ for both the average and maximum distributions, indicating greater membrane wrinkling in the region of contact. The pattern of membrane separations observed represents the freezing of membrane undulatory motions of the vesicle membrane when it adhered to the planar membrane.

punctate attachment sites was rare, <15% of the region of contact was characterized by pixel-to-pixel changes in separation >3 nm. Thus, increased $[Ca^{2+}]$ caused the membranes to become closer by pinning them together at more attachment sites. Membranes in the contact region became permanently wrinkled due to these close attachments.

DISCUSSION

The Use of RET Optical Microscopy to Study Membrane Interactions

The close approach of two phospholipid bilayer membranes is the first stage in the sequence of reactions leading to fusion (Akabas et al., 1984; Niles and Cohen, 1987). We have used RET imaging video microscopy to discern structural features of the stable adhesion of large lipid vesicles to planar membranes, which may be important for membrane fusion. The information provided by RET microscopy is a two-dimensional spatial map of the distances of separation between the headgroups of the two membranes. The accuracy of the intermembrane separation distances is limited by the ability to calibrate RET in the specimen (Niles and Cohen, 1995). The two-dimensional localization of intermembrane separation distances is ultimately limited by both optical diffraction and the digitization rate of image processing. The two-point resolution of our system is ~0.75 μm, as determined by the roll-off of the modulation transfer function (Niles and Cohen, 1995). This makes the effective diameter of the point-spread function at half-maximum intensity ~0.4 μm, while the width of a digitized pixel is 0.488 μm, so that individual image points are localized to individual pixels. The spillover of point-spread function amplitudes into adjacent pixels, and the lack of registration between image points and the centers of pixels, however, cause subresolution features in the image to be delocalized. Thus, the area resolution of the region of vesicle-planar membrane contact is confined to a relatively low range of spatial frequencies, defined by a length of ~0.5 μm. Our rather low spatial resolution map of the region of vesicle-planar membrane contact (at separation distances >1 nm) shows the interaction to be more complex than previously suspected.

We chose coumarin and rhodamine as the dye pair because the R_0 is relatively small, ~3.2 nm due to small spectral overlap, placing it within the range of expected intermembrane separation distances. Energetic interactions between membranes are significant at distances less than 5 nm, and the force regimes that produce large disjoining pressures (forces that oppose close approach) typically attain very large values at distances <2 nm (Rand and Parsegian, 1984; McIntosh

and Simon, 1986). Our choice of probes ensured that $\Delta I_A/I_D$ varied reliably over this range of separation distances and was not confined to an extreme range (Drake et al., 1991). We calibrated RET under circumstances designed to account for the major source of error, self-quenching of acceptor fluorescence (Ludwig et al., 1992), so that the experimentally validated R_0 enabled intermembrane separations >1 nm to be reliably measured. To study membrane interactions such as the adhesion and fusion of biological membranes, different RET probe pairs will prove more efficacious. For example, cell–cell interactions are limited by a 10–20 nm-thick glycocalyx (Hammer and Lauffenburger, 1989) and will require a dye pair with a longer critical distance, although the methodology adopted in this study can readily be applied to biological membranes. In addition, suitable probe pairs can be found to study interactions between different parts of phospholipid molecules, such as interactions between hydrocarbon domains during fusion. The dyes utilized in this study were ideal for studying the stable adhesion between membranes because they were located on the headgroups of phospholipids and probed the aqueous environment between the membranes. For studies of membrane fusion and its structural intermediates, hydrophobic probes attached to aliphatic chains will prove most feasible. The hydrocarbon environment provides a three-dimensional space in which the probes interact and allows a greater RET signal due to an increased number of combinatorial interactions (Kuhn, 1970; Estep and Thompson, 1979; Wolber and Hudson, 1979; Dewey and Hammes, 1980). The headgroup-localized coumarin-rhodamine pair is poorly suited for membrane fusion studies. As long as the headgroup probes are located on separate planes, k_t varies with the fourth power of separation, according to Eq. 4a. When the probes located on fusing monolayers start to mix, they interact within the two dimensions of a single plane, and k_t reverts to variation with the inverse sixth power of separation.[2]

Vesicle-Planar Membrane Binding and [Ca^{2+}]

This study reveals the presence of large gaps between the headgroups of the vesicle and planar membranes on the order of 1–6 nm. This and other structural features of the region of contact explain several phenomena encountered in this model system of exocytosis. The osmotic gradients experimentally required for fusion (Cohen et al., 1989) were always predicted to generate hydrostatic pressures much greater than those necessary to rupture or lyse the membranes, with the assumption that all the water flow across the planar membrane in the region of contact entered the vesicle (Woodbury and Hall, 1988; Niles et al., 1989; Cohen and Niles, 1993). One explanation offered was that the adherent vesicle and planar membranes remained separated by a gap or corridor and that most of the water flow generated by the osmotic gradient across the planar membrane was shunted around rather than into the vesicle (Akabas et al., 1984). A comparison of the osmotic gradient necessary to produce membrane lysis with the osmotic gradient experimentally required for fusion resulted in an estimated gap width of 5 nm with μm-diameter vesicles (Niles and Cohen, 1991). In fact, this study shows that the membranes are separated by >1 nm in most of the contact region, and only a small proportion of the contact area is separated by a gap less than 2 nm. We have found that the gaps are large enough to accommodate large osmotic water flows. The water flow into the gap creates a hydrostatic pressure within the corridor, which, in turn, drives water into the vesicle as well as around it. The intravesicular hydrostatic pressure expected with an intermembrane gap is adequate to induce fusion (Niles et al., 1989).

Structural details in the area of contact revealed by RET microscopy account for the strong Ca^{2+}-mediated adhesion of vesicles to planar membranes found in earlier studies (Akabas et al., 1984; Niles and Eisenberg, 1985). One of the most striking features in the contact region is the presence of punctate attachment sites, where small localized areas of the two bilayers are pulled to within separation distances ≤2 nm. Although the total area of the contact region as a function of [Ca^{2+}] is biphasic (Fig. 7 *B*), consistent with the known electrostatic behavior of divalent cation interactions with anionic membranes (McLaughlin et al., 1981), the density of punctate sites is the one feature that increases with [Ca^{2+}]. The proportion of the region of contact comprising these sites is small (Fig. 7 *B*), but their [Ca^{2+}] dependence, in contrast to that of the total area of the region of contact, parallels both the number of vesicles bound to the planar membrane (Niles and Cohen, 1987, 1991) and the rate of membrane fusion (Zimmerberg et al., 1980; Niles, unpublished data). This suggests that the adhesion interaction is strongest at the punctate attachment sites; we envision that fusion is initiated at these sites, where membranes are closest.

Adhesion at Punctate Sites

We propose that the punctate attachment sites are localized regions where the Ca^{2+} has bound two anionic phospholipids such as PS, one each from the facing monolayers of the two membranes, to form cross-

[2]This can be seen from the theoretical development of Eq. 4a given in the legend of Fig. 1 *B*. When the donor and acceptor probes interact in a single plane, the angle Θ between the radial vector **R** and the bilayer normal is no longer swept from 0 to $\pi/2$ but remains fixed at $\pi/2$, and k_t is determined by the radial distribution function of acceptors relative to each donor (Estep and Thompson, 1979).

bridges between the membranes and a site of small intermembrane separation (Portis et al., 1979). Although individual $Ca(PS)_2$ cross-bridges are too small to be spatially resolved by any optical system, the punctate attachment sites could be localized regions where a large number of cross-bridges have formed to create a relatively large domain of closely apposed two membranes. As a single square pixel in our ratio images represents an area of $\sim 2.38 \times 10^5$ nm^2 containing $\sim 1.42 \times 10^5$ phospholipids in each monolayer, at 16 mol% PS, a single punctate attachment site could contain as many as 23,000 $Ca(PS)_2$ cross-bridges (ignoring lateral phase separation). Lateral aggregation into $Ca(PS)_2$-rich domains would increase this number. While the acceptor probe might be excluded from these domains, the dye-labeled PEs are negatively charged and, therefore, could participate in cross-bridge formation. The variation of the sensitization ratio with the phase state of the lipids is unknown, although coumarin is much less sensitive to environmental perturbation than probes such as bimane and NBD (Silvius et al., 1987). Moreover, we did not observe Ca^{2+}-dependent aggregation of the fluorophores. The phase state of the punctate attachment sites remains uncertain. Vesicles initially adsorbed to planar membranes in mM $[Ca^{2+}]$ did not subsequently detach when $[Ca^{2+}]$ was lowered (to ~ 10 μM) by the addition of EDTA. This is suggestive of $Ca(PS)_2$ complex formation with equilibrium dissociation constants in the micromolar to nanomolar range as observed in complexes formed in fully hydrated multilayers of PS in ion-free water (Feigenson, 1986, 1989), although these complexes result in phase separation (Coorssen and Rand, 1995) and the electrolyte conditions are different. It is possible that vesicle attachment is hindered by hydrodynamic forces due to propulsion and the convection of the bathing solution, so that formation of the contact region does not occur under equilibrium conditions. The $[Ca^{2+}]$ dependence of the formation of the contact region may be determined by divalent cation absorption to single bilayers, with K_d's in the tens of millimolar range, which does not result in phase separation (McLaughlin et al., 1981).

The spatial order of the arrangement of attachment sites within each contact region determined in the autocorrelation images could arise by formation of a structural phase domain. If the submicroscopic ordering within a site scaled to optically resolvable lengths, then site formation would be analogous to crystallization phenomena. But this would produce a continuous two-dimensional correlation function (Reichl, 1980), which we did not observe. The regular pattern in the contact region could arise by a superimposed mechanical constraint, such as an increased rigidity due to Ca^{2+} binding. The reduced flexibility of the membrane would prevent the formation of adjacent attachment sites, and effectively "comb" the correlation function into the discrete pattern observed. In any case, it is clear that the attachment sites are related to membrane adhesion. To understand their possible roles in the membrane rearrangements of fusion, it is worthwhile to examine the forces between membranes and the stresses that close apposition imparts to lipid bilayers.

Forces between Membranes

Adhesion between membranes represents a balance of attractive and repulsive forces that is biased toward the attractive forces (Parsegian and Rand, 1983). The work of close approach is the integral of the force required to bring the two membranes from infinite separation to a particular distance. Therefore, the spatial map of intermembrane distances represents the energy profile of the region of contact, and we can estimate the magnitude of the adhesion force from the magnitudes of the repulsive forces. Some of these pressures (force per unit area) as a function of distance from a fixed membrane surface are plotted in Fig. 10 *A*. We chose the interface between the aqueous milieu and the lipid headgroups as our plane of reference, because this was the most probable location of our RET probes, and we refer our distances to this plane. The largest repulsive force between membranes originates from the steric interaction of the headgroups, which is 0 at separations where the headgroups do not overlap (Israelachvili and Wennerström, 1992). Because we confined our calibrated measurements of intermembrane separation to ≥ 1 nm, the contribution of the steric pressure was very small. The most significant disjoining pressures at distances ≥ 1 nm are hydration (*open boxes*) of the polar headgroups of the lipids (LeNeveu et al., 1976; Parsegian and Rand, 1983; McIntosh and Simon, 1986) and electrostatic repulsion (*filled boxes*) between the negatively charged headgroups of the apposed bilayers (Evans and Ipsen, 1991). These forces predominate at distances <2 nm, where they exceed the attractive Van der Waals interaction (*triangles*) between the hydrocarbon tails of phospholipid molecules across the intervening aqueous milieu, which mediates adhesion at separations where $Ca(PS)_2$ cross-bridges are unable to form. At distances >2 nm, repulsion is dominated by fluctuation-induced interactions, which originate from the entropic confinement of thermally induced changes in the shape and local geometry of flexible, unpressurized membranes (Helfrich, 1978). The most significant of these interactions arises from local curvature fluctuations (*circles*) that produce undulations of the membrane surface, or luffing. When membranes are brought close together, the amplitudes of these undulations are decreased, confining these motions to particular spatial modes, and the damped modes propel

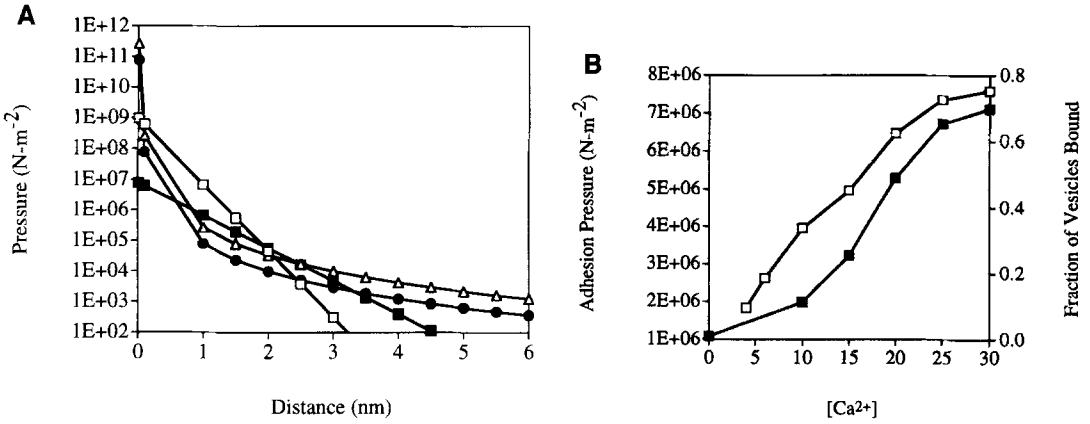

FIGURE 10. Intermembrane forces in the region of vesicle-planar membrane contact. (*A*) The magnitudes of various forces between membranes, expressed as pressures (area-normalized force). The hydration repulsion pressure (*open boxes*) declines as $P_0e^{-a/\lambda}$, where P_0 is 10^9 *N-m*$^{-2}$ and the decay length λ is 0.2 nm (Parsegian and Rand, 1983; McIntosh and Simon, 1986). The electrostatic repulsion pressure (*filled boxes*) between flat membranes bathed in electrolyte is $2\sigma s^2e^{-\kappa a}/\epsilon\epsilon_0$, where the surface charge density σ is 0.0534 C/*m*^{2} for 20% anionic membranes, the dielectric constant ϵ is 80, the dielectric permittivity of vacuum ϵ_0 is 8.854×10^{-12} C^2/*J-m*, and the Debye length $1/\kappa$ was approximated as 0.4 nm for 15 mM $CaCl_2$ (Israelachvili, 1986). The attractive Van der Waals interaction (*open triangles*) is -5×10^{-21} $J/12\pi a^3$ (Israelachvili, 1991). The undulation pressure (*filled circles*) is $3\pi^2(kT)^2/64K_ba^3$, where the elastic bending modulus of the membrane $K_b \sim 10^{-19}$ *J* (Helfrich, 1978). (*B*) Lower limits of the adhesion pressure in the region of contact necessary to overcome the disjoining pressures as a function of [Ca^{2+}] (*open boxes*). The adhesion pressure at each concentration was calculated by summing the hydration and undulation pressures at each intermembrane separation distance, weighting the summed pressure by the fraction of the contact area occupied by membranes with the same separation distance, and then summing the weighted pressures over all intermembrane separations. The fraction of vesicles encountering a planar membrane that bind is shown as a function of [Ca^{2+}] for comparison (*filled boxes*).

the membranes apart (Evans and Parsegian, 1986; Lipowsky and Leibler, 1986; Evans and Ipsen, 1991; Podgornik and Parsegian, 1992). The spatial profile of the intermembrane separations in the contact region that we have observed exhibits characteristics expected for the confinement of undulatory membrane motions.

We used the magnitudes of these forces to estimate the lower bound of the adhesion pressure (the attractive force per unit area) in the region of contact by assuming that the adhesion pressure is equal to or greater than the disjoining pressure. The adhesion pressures that must be exerted between the membranes in the region of contact to allow the membranes to reach the measured separations are shown in Fig. 10 *B* (*open boxes*). At each separation distance, the adhesion pressure was estimated as the sum of the hydration and undulation pressures. We neglected the electrostatic pressure because, under our experimental conditions, it had significantly decayed by 2 nm. Both the hydration and electrostatic repulsive force calculations assume flat membranes. These forces become longer ranged due to undulation (Lipowsky and Leibler, 1986; Evans and Ipsen, 1991) and, canonically, cannot be simply added to obtain the total force. (The hydration pressures are experimentally determined, and therefore, contain contributions from undulations. In fact, the direct forces of hydration may well extend over only several water layers with undulations accounting for the observed long range repulsion.) Nonetheless, because the hydration pressure decays exponentially over a short range of distances while the undulation pressure decays more gradually, our approximation of the net disjoining pressure as a sum accounts for the changes in the nature of the repulsive force at 2 nm separation. We weighted our calculated net pressure by the relative area of the contact region at the intermembrane separation distance and summed over all intermembrane separations in the contact region. The adhesion pressure is proportional to [Ca^{2+}] and varies by about a factor of five over the range of 4–30 mM, indicating that both cross-bridge formation and electrostatic screening participate in adhesion. The [Ca^{2+}] dependence of the adhesion pressure resembles that of both the number of vesicles bound to the planar membrane (*filled boxes*), as well as the proportion of the contact area with intermembrane separations $\leq$1.3 nm (Fig. 7 *B*), supporting our conclusion that the areas of close apposition provide most of the adhesive force in the region of contact.

The repulsive forces between membranes also allow estimation of a lower bound to the strength of adhesive forces in the punctate attachment sites. At intermembrane distances 1 to 2 nm, the adhesion pressure is $>10^6$ *N-m*$^{-2}$, corresponding to a force in each punctate attachment site $>2.4 \times 10^{-7}$ *N*. If this force is distributed evenly among 23,000 $Ca(PS)_2$ cross-bridges in the site, then each cross-bridge must provide an adhesion force of at least 10 pN to balance the disjoining force. If the cross-bridges are aggregated within the punctate at-

tachment sites, then the adhesion force per cross-bridge is correspondingly smaller. The magnitude of this force is typical of intermolecular forces of strong adhesion. For example, the swivel of an actin-myosin cross-bridge generates a force of 3-4 pN (Svoboda et al., 1994), and the adhesive force between biotin and streptavidin, with a stability constant of 10^{14} M, is between 80 and 250 pN, depending on the pH (Moy et al., 1994). Strong adhesion forces are correlated with large equilibrium association constants. The binding of divalent cations to oxyanion groups is very strong, as the stability constants for Ca^{2+} association with unprotonated sites in the iminodiacetate moieties of EGTA and EDTA are $\sim 10^{11}$ M, and for divalent cations with hydroxyl anions are $\sim 10^{9}$ M^{-1} (Martell and Smith, 1974). Our estimate of the binding force at the attachment sites is consistent with the large stability constants ranging 10^{6}–10^{9} M for $Ca(PS)_2$ in fully hydrated multilayers in the absence of other salts (Feigenson, 1986, 1989).

The repulsive interaction induced by the damping of undulation modes provides a large tendency for the membranes to separate in the region of contact. The extent of this damping can be appreciated by comparing the amplitude of an undulation expected for the free, thermal motion of a flexible membrane with the changes in intermembrane separation measured in the region of contact. The energy of an undulation mode is the curvature energy of the patch of membrane, $E = 1/2\ K_b\ (2/R)^2 \cdot$ area, where K_b is the elastic bending modulus and R is the radius of curvature of the mode (we assume that the intrinsic curvature of the membrane is 0) (Helfrich, 1973). If we circularize a square pixel with an edge length of 488 nm, the spatial resolution of our image processing, then the radius of the same area, r, is 275 nm and the area is 0.238 μm^2. For an undulation with thermal energy kT, the radius of curvature of the mode is 3.41 μm ($R = \sqrt{2K_b/kT \cdot \text{area}}$), and, since the area of the mode is approximately equal to $2\pi Ra$, where a is the amplitude, the expected pixel-to-pixel change in separation between the membranes is 11.1 nm. For a larger square area of 100 pixels (23.8 μm^2) with $r = 2.75$ μm, $R = 34.1$ μm, and the amplitude of the 1 kT luff is 111 nm. As the pixel-to-pixel changes in intermembrane separation across the region of contact are confined to amplitudes <5 nm (Figs. 9, *A* and *B*), the undulation force is largely suppressed by adhesion. This indicates that the residual pattern observed is the "frozen" remnant of a freely luffing membrane that has become strongly attached to a surface (the planar membrane), resistant to thermally induced changes in curvature.

Energies of Punctate Attachment Sites and Monolayer Fusion

While the punctate attachment sites are the structural feature of the region of contact most significantly associated with adhesion in the vesicle-planar membrane system, what are their roles in fusion? Besides providing a strong attachment of the two membranes, the sites may also distort the membrane surface into prefusion structures that reduce the free energy barrier to the formation of structural intermediates of membrane fusion. The conceptual structure most studied has been the "stalk" in which the facing monolayers of the two membranes are melded or hemifused into a highly curved single monolayer connecting the two membranes (Chernomordik et al., 1985). The smallest stalk that can be geometrically formed between two membranes separated by a 3-nm distance has a hydrocarbon domain diameter (skirt) of 3 nm, and a curvature radius at the headgroup-aliphatic tail interface of 1.5 nm. The outer surface of this simple stalk is geometrically identical to the surface lining the hole of a torus, and its area (61 nm^2) contains $\sim$100 lipid molecules. The curvature energy required to bend two flat lipid bilayers into the stalk is $\sim$30 kT (Siegel, 1993). The microscopic structures producing the punctate attachment sites can be schematized as collections of partial stalks that are spatially symmetric bulgings of the facing monolayers of the two membranes into the intervening space. If the nearest approach of the bulge crests is 1 nm, then this is equivalent to a simple stalk with a 1 nm long region of the central skirt region removed. The removed skirt contains 16 lipid molecules, but the areas of the newly exposed surfaces (the tops of the bulges) can accommodate 26 lipid molecules, in addition to the 84 molecules remaining on the sides of the bulges. Thus, two bulges contain 110 lipid molecules compared to 100 molecules in the stalk. Because the original circular areas under the stalk contained 94 lipid molecules, the bulges serve to accumulate lipid molecules as required to form a stalk. The curvature energy of the bulges is $\sim$10 kT, and $\sim$20 kT is still required to bend the molecules into a complete stalk. Independently of the precise numbers, Ca^{2+}-dependent cross-bridge formation leads to bulges and the curvature energy required to form a hemifused stalk is decreased: The lipid molecules lining the sides of the bulges are already curved in a direction favorable for the formation of the stalk. Therefore, the punctate attachment sites may contribute to the free energy necessary to form the intermediate structures of membrane fusion.

Supported by NIH GM27367.

Original version received 2 August 1995 and accepted version received 6 December 1995.

REFERENCES

Akabas, M.H., F.S. Cohen, and A. Finkelstein. 1984. Separation of the osmotically driven fusion event from vesicle-membrane attachment in a model system for exocytosis. *J. Cell Biol.* 98:1063–1071.

Bennett, M.K., and R.H. Scheller. 1993. The molecular machinery for secretion is conserved from yeast to neurons. *Proc. Natl. Acad. Sci.* 90:2559–2563.

Brand, L., and B. Witholt. 1967. Fluorescence measurements. *Methods Enzymol.* 11:776–856.

Campbell, I.D., and R.A. Dwek. 1981. Fluorescence. *In* Biological Spectroscopy. The Benjamin/Cummings Publishing Co., Inc., Menlo Park, CA. 91–125.

Chernomordik, L.V., M.M. Kozlov, G.B. Melikyan, I.G. Abidor, V.S. Markin, and Y.A. Chizmadzhev. 1985. The shape of lipid molecules and monolayer membrane fusion. *Biochim. Biophys. Acta.* 812:643–655.

Chernomordik, L.V., A.N. Chanturya, J. Green, and J. Zimmerberg. 1995. The hemifusion intermediate and its conversion to complete fusion: Regulation by membrane composition. *Biophys. J.* 69:922–929.

Cohen, F.S., J. Zimmerberg, and A. Finkelstein. 1980. Fusion of phospholipid vesicles with planar phospholipid bilayer membranes II. Incorporation of a vesicular membrane marker into the planar membrane. *J. Gen. Physiol.* 75:251–270.

Cohen, F.S., M.H. Akabas, and A. Finkelstein. 1983. Association and fusion of phospholipid vesicles to planar lipid membranes. *Biophys. J.* 41:29*a*. (Abstr.)

Cohen, F.S., W.D. Niles, and M.H. Akabas. 1989. Fusion of phospholipid vesicles with a planar phospholipid membrane depends on the membrane permeability of the solute used to create the osmotic pressure. *J. Gen. Physiol.* 93:201–210.

Cohen, F.S., and W.D. Niles. 1993. Reconstituting channels into planar membranes: a conceptual framework and methods for fusing vesicles to planar bilayer phospholipid membranes. *Methods Enzymol.* 220:50–68.

Coorssen, J.R., and R.P. Rand. 1995. Structural effects of neutral lipids on divalent cation-induced interactions of phosphatidylserine-containing bilayers. *Biophys. J.* 68:1009–1018.

Dale, R.E., and J. Eisinger. 1974. Polarized excitation energy transfer. *In* Biochemical Fluorescence: Concepts. R.F. Chen and H. Edelhoch, editors. Marcel Dekker, Inc., New York. 115–284.

Dale, R.E., J. Eisinger, and W.E. Blumberg. 1979. The orientational freedom of molecular probes: the orientation factor in intramolecular energy transfer. *Biophys. J.* 26:161–194.

Dewey, T.G., and G.G. Hammes. 1980. Calculation of fluorescence resonance energy transfer on surfaces. *Biophys. J.* 32:1023–1036.

Drake, J.M., J. Klafter, and P. Levitz. 1991. Chemical and biological microstructures as probes of dynamic processes. *Science (Wash. DC).* 251:1574–1579.

Estep, T.N., and T.E. Thompson. 1979. Energy transfer in lipid bilayers. *Biophys. J.* 26:195–208.

Evans, E.A., and V.A. Parsegian. 1986. Thermal-mechanical fluctuations enhance repulsion between bimolecular layers. *Proc. Natl. Acad. Sci. USA.* 83:7132–7136.

Evans, E.A., and R. Waugh. 1977. Mechanochemistry of closed, vesicular membrane systems. *J. Coll. Interface Sci.* 60:286–323.

Evans, E.A., and J. Ipsen. 1991. Entropy-driven expansion of electric double layer repulsion between highly flexible membranes. *Electrochimica Acta.* 36:1735–1741.

Feigenson, G.W. 1986. On the nature of calcium ion binding between phosphatidylserine lamellae. *Biochemistry.* 25:5819–5825.

Feigenson, G.W. 1989. Calcium ion binding between lipid bilayers: the four-component system of phosphatidylserine, phosphatidylcholine, calcium chloride, and water. *Biochemistry.* 28:1270–1278.

Förster, Th. 1948. Intermolecular energy migration and fluorescence. *Annalen der Physik.* 2:55–75. Translated from German by R.S. Knox, Department of Physics and Astronomy, University of Rochester, as Biological Physics Group Technical Report 46.

Gibson, G.A., and L.M. Loew. 1979. Application of Förster resonance energy transfer to interactions between cell or lipid vesicle surfaces. *Biochem. Biophys. Res. Commun.* 88:141–146.

Hammer, D.A., and D.A. Lauffenburger. 1989. A dynamical model for receptor-mediated cell adhesion to surfaces in viscous shear flow. *Cell Biophys.* 14:139–173.

Helfrich, W. 1973. Elastic properties of lipid bilayers: Theory and possible experiments. *Zeitschrift fur Naturforschung.* 28:693–703.

Helfrich, W. 1978. Steric interaction of fluid membranes in multilayer systems. *Zeitschrift fur Naturforschung.* 33:305–315.

Helm, C.A., J.N. Israelachvili, and P.M. McGuiggan. 1992. Role of hydrophobic forces in bilayer adhesion and fusion. *Biochemistry.* 31:1794–1805.

Herman, B. 1989. Resonance energy transfer microscopy. *Methods Cell Biol.* 30:219–243.

Hoekstra, D., T. de Boer, K. Klappe, and J. Wilschut. 1984. Fluorescence method for measuring the kinetics of fusion between biological membranes. *Biochemistry.* 23:5675–5681.

Israelachvili, J.N. 1991. Intermolecular and Surface Forces, 2nd ed. Academic Press, New York, 265–266.

Israelachvili, J.N., and H. Wennerström. 1992. Entropic forces between amphiphilic surfaces in liquids. *J. Phys. Chem.* 96:520–531.

Kim, S., and G.M. Martin. 1981. Properties of cell-size unilamellar liposomes with high captured volume and defined size distribution. *Biochim. Biophys. Acta.* 646:1–9.

Kuhn, H. 1970. Classical aspects of energy transfer in molecular systems. *J. Chem. Phys.* 53:101–108.

LeNeveu, D.M., R.P. Rand, and V.A. Parsegian. 1976. Measurement of forces between lecithin bilayers. *Nature (Lond.).* 259:601–603.

Lipowsky, R. 1991. The conformation of membranes. *Nature (Lond.).* 349:475–481.

Lipowsky, R., and S. Leibler. 1986. Unbinding transitions of interacting membranes. *Phys. Rev. Lett.* 56:2541–2544.

Ludwig, M., N.F. Hensel, and R.J. Hartzman. 1992. Calibration of a resonance energy transfer imaging system. *Biophys. J.* 61:845–857.

McLaughlin, S., N. Mulrine, T. Gresalfi, G.Vaio, and A. McLaughlin. 1981. Adsorption of divalent cations to bilayer membranes containing phosphatidylserine. *J. Gen. Physiol.* 77:445–473.

MacDonald, R.I. 1990. Characteristics of self-quenching of the fluorescence of lipid-conjugated rhodamine in membranes. *J. Biol. Chem.* 265:13533–13539.

Martell, A., and R.M. Smith. 1974. Critical stability constants. Vols. 1 and 4. Plenum Publishing Corp., NY.

Massari, S., R. Colonna, and E. Folena. 1988. Interaction of the fluorescent probe *N*-(lissamine Rhodamine B sulfonyl)dipalmitoylphosphatidylethanolamine with phosphotidylcholine bilayers. *Biochim. Biophys. Acta.* 940:149–157.

McIntosh, T.J., and S.A. Simon. 1986. Hydration force and bilayer deformation: a reevaluation. *Biochemistry.* 25:4058–4066.

Montal, M., and P. Mueller. 1972. Formation of bimolecular membranes from lipid monolayers and a study of their electrical properties. *Proc. Natl. Acad. Sci. USA.* 69:3561–3566.

Moy, V.T., E.L. Florin, and H.E. Gaub. 1994. Intermolecular forces and energies between ligands and receptors. *Science (Wash. DC).* 266:257–259.

Needham, D., and D.A. Haydon. 1983. Tensions and free energies of formation of "solventless" lipid bilayers. *Biophys. J.* 41:251–257.

Niles, W.D., and M. Eisenberg. 1985. Fluorimetric detection of

phospholipid vesicles bound to planar phospholipid membranes. *Biophys. J.* 48:321–325.

Niles, W.D., and F.S. Cohen. 1987. Video fluorescence microscopy studies of phospholipid vesicle fusion with a planar phospholipid membrane. *J. Gen. Physiol.* 90:703–735.

Niles, W.D., F.S. Cohen, and A. Finkelstein 1989. Hydrostatic pressures developed by osmotically swelling vesicles bound to planar membranes. *J. Gen. Physiol.* 93:211–244.

Niles, W.D., and F.S. Cohen 1991. Video microscopy studies of vesicle-planar membrane adhesion and fusion. *In* Calcium Entry and Action at the Presynaptic Nerve Terminal. E.F. Stanley, D.J. Triggle, and M.C. Nowicky, editors. *Ann. NY Acad. Sci.* 635:285–297.

Niles, W.D., J. Silvius, and F.S. Cohen. 1993. Resonance energy transfer microscopy applied to membrane fusion. *Biophys. J.* 64: A235. (Abstr.)

Niles, W.D., and F.S. Cohen. 1995. Radiometric calibration of a video fluorescence microscope for the quantitative imaging of resonance energy transfer. *Rev. Sci. Instr.* 66:3527–3536.

Parsegian, V.A., and R.P. Rand. 1983. Membrane interaction and deformation. *Ann. NY Acad. Sci.* 416:1–12.

Perin, M.S., and R.C. MacDonald. 1989. Interaction of liposomes with planar bilayer membranes. *J. Membr. Biol.* 109:221–232.

Podgornik, R., and V.A. Parsegian. 1992. Thermal-mechanical fluctuations of fluid membranes in confined geometries: the case of soft confinement. *Langmuir.* 8:557–562.

Portis, A., C. Newton, W. Pangborn, and D. Papahadjopoulos. 1979. Studies on the mechanism of membrane fusion: evidence for an intermediate Ca^{2+}-phospholipid complex, synergism with Mg^{2+}, and inhibition by spectrin. *Biochemistry.* 18:780–790.

Reichl, L.E. 1980. A Modern Course in Statistical Physics. University of Texas Press, Austin, TX. 314–347.

Ruelle, D. 1989. Elements of Differentiable Dynamics and Bifurcation Theory. Academic Press, Inc., Boston, MA. 37–48.

Russ, J.C. 1992. The Image Processing Handbook. The CRC Press. Boca Raton, FL. 125–134.

Schiller., P.W. 1974. The measurement of intramolecular distances by energy transfer. *In* Biochemical Fluorescence: Concepts. R.F. Chen and H. Edelhoch, editors. Marcel Dekker, Inc., New York. 285–303.

Siegel, D. 1993. Energetics of intermediates in membrane fusion: comparison of stalk and inverted micellar intermediate mechanisms. *Biophys. J.* 65:2124–2140.

Silvius, J.R., R. Leventis, P.M. Brown, and M. Zuckermann. 1987. Novel fluorescent phopholipids for assays of lipid mixing between membranes. *Biochemistry.* 26:4279–4287.

Snyder, B., and E. Friere. 1982. Fluorescence energy transfer in two dimensions: a numeric solution for random and nonrandom distributions. *Biophys. J.* 40:137–148.

Stryer, L. 1978. Fluorescence energy transfer as a spectroscopic ruler. *Annu. Rev. Biochemistry.* 47:819–846.

Svoboda, K., P.P. Mitra, and S.M. Block. 1994. Fluctuation analysis of motor protein movement and single enzyme kinetics. *Proc. Natl. Acad. Sci. USA.* 91:11782–11786.

Szoka, F., and D. Papahadjopoulos. 1980. Comparative properties and methods of preparation of lipid vesicles. *Annu. Rev. Biophys. Bioeng.* 9:462–508.

White, J.M. 1992. Membrane fusion. *Science (Wash. DC).* 258:917–924.

Wolber, P.K., and B.S. Hudson. 1979. An analytic solution to the Förster energy transfer problem in two dimensions. *Biophys. J.* 28: 197–210.

Woodbury, D.J., and J.E. Hall. 1988. Role of channels in the fusion of vesicles with a planar bilayer. *Biophys. J.* 54:1053–1063.

Zimmerberg, J., F.S. Cohen, and A. Finkelstein. 1980. Fusion of phospholipid vesicles with planar phospholipid bilayer membranes. I. Discharge of vesicular contents across the planar membrane. *J. Gen. Physiol.* 75:241–250.

Zimmerberg, J., S.S. Vogel, and L.V. Chernomordik. 1993. Mechanisms of membrane fusion. *Annu. Rev. Biophys. Biomol. Struct.* 22: 433–466.